Article

Current Biology

Competition for Space Is Controlled by Apoptosis-Induced Change of Local Epithelial Topology

Graphical Abstract

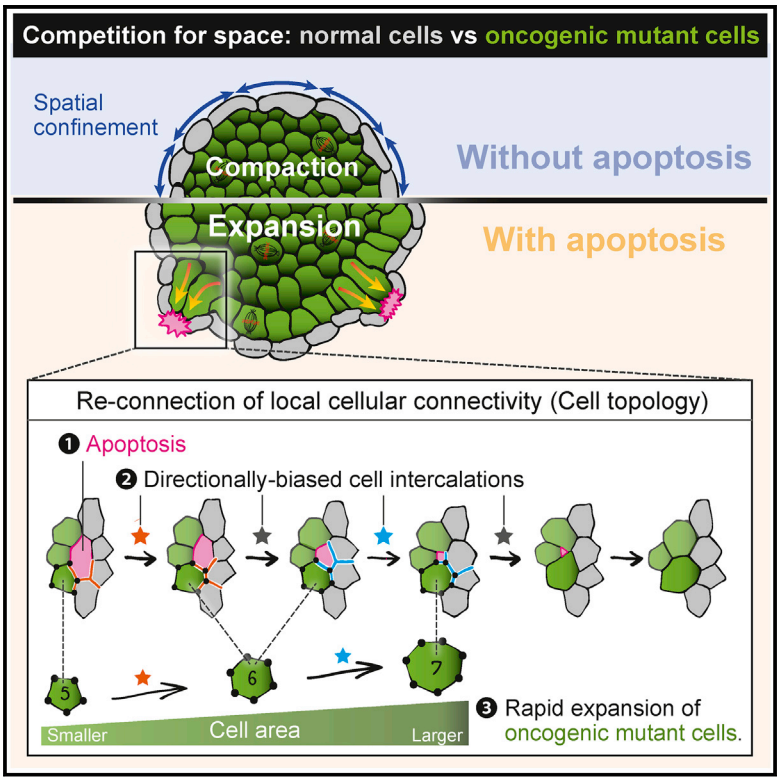

Highlights

- Rapid cell expansion of oncogenic mutants fills space of normal cell apoptosis
- Topological change by directionally biased cell intercalations drives cell expansion
- The topological dynamics is verified with *in silico* and *in vivo* experiments
- Repetitive rapid cell turnover via topological changes accelerates mutant expansion

Authors

Alice Tsuboi, Shizue Ohsawa, Daiki Umetsu, Yukari Sando, Erina Kuranaga, Tatsushi Igaki, Koichi Fujimoto

Correspondence

fujimoto@bio.sci.osaka-u.ac.jp

In Brief

Tsuboi et al. investigate the spatiotemporal evolution of cell turnover during cell competition. Winner cells compensate for the space of losers' apoptosis by rapid cell expansion through re-connection of local cellular connectivity (topology). This topology dynamics may drive the pathological development initiated from an oncogenic mutation.

Tsuboi et al., 2018, Current Biology *28*, 2115–2128
July 9, 2018 © 2018 The Author(s). Published by Elsevier Ltd.
https://doi.org/10.1016/j.cub.2018.05.029

CellPress

Current Biology
Article

Competition for Space Is Controlled by Apoptosis-Induced Change of Local Epithelial Topology

Alice Tsuboi,[1] Shizue Ohsawa,[2] Daiki Umetsu,[3] Yukari Sando,[2] Erina Kuranaga,[3] Tatsushi Igaki,[2] and Koichi Fujimoto[1,4,*]
[1]Graduate School of Sciences, Osaka University, Toyonaka 560-0043, Japan
[2]Graduate School of Biostudies, Kyoto University, Kyoto 606-8501, Japan
[3]Graduate School of Life Sciences, Tohoku University, Sendai 980-8577, Japan
[4]Lead Contact
*Correspondence: fujimoto@bio.sci.osaka-u.ac.jp
https://doi.org/10.1016/j.cub.2018.05.029

SUMMARY

During the initial stage of tumor progression, oncogenic cells spread despite spatial confinement imposed by surrounding normal tissue. This spread of oncogenic cells (winners) is thought to be governed by selective killing of surrounding normal cells (losers) through a phenomenon called "cell competition" (i.e., supercompetition). Although the mechanisms underlying loser elimination are increasingly apparent, it is not clear how winner cells selectively occupy the space made available following loser apoptosis. Here, we combined live imaging analyses of two different oncogenic clones (Yki/YAP activation and Ras activation) in the *Drosophila* epithelium with computer simulation of tissue mechanics to elucidate such a mechanism. Contrary to the previous expectation that cell volume loss after apoptosis of loser cells was simply compensated for by the faster proliferation of winner cells, we found that the lost volume was compensated for by rapid cell expansion of winners. Mechanistically, the rapid winner-dominated cell expansion was driven by apoptosis-induced epithelial junction remodeling, which causes re-connection of local cellular connectivity (cell topology) in a manner that selectively increases winner apical surface area. *In silico* experiments further confirmed that repetition of loser elimination accelerates tissue-scale winner expansion through topological changes over time. Our proposed mechanism for linking loser death and winner expansion provides a new perspective on how tissue homeostasis disruption can initiate from an oncogenic mutation.

INTRODUCTION

Primary tumors originate from a single transformed cell containing oncogenic mutations despite being spatially confined by surrounding normal tissue. It is increasingly apparent that oncogenic cell spread within tissue is driven not only simply by a higher rate of proliferation, but also by a phenomenon called "cell competition" [1, 2]. Cell competition is a process in which "winner" cells take over the tissue at the expense of neighboring "loser" cells [1–7]. When oncogenic mutant cells act as winners, the mutant cells eliminate surrounding normal wild-type cells by inducing apoptosis, and thus spread their territory. Because inhibiting loser apoptosis is sufficient to halt winner spread [1, 2, 5, 8, 9], loser apoptosis seems to play an active role in promoting winner spread within the tissue. However, it is unclear how loser apoptosis impacts surrounding cells to produce selective occupation by winner cells.

Cell competition can be considered as processes of destruction (loser apoptosis) and reconstruction (winner takeover) of the epithelial tissue structure [1–20]. Epithelial tissue consists of a sheet of tightly packed cells connected with adhesive junctions. This local cell-cell connectivity ("cell topology" [21, 22]) is represented by a distribution of the number of sides (adherent neighbors) of each cell. Because the side number positively correlates with the apical surface area (known as Lewis's law conserved in epithelial tissue [22, 23]), topological change is associated with cellular expansion or contraction. In the case of cell competition, the topology of neighboring cells could be changed through loser cell delamination or extrusion, which associates consecutive junctional remodeling (cell intercalation) between a dying cell and its surviving neighbors [7, 24]. Topological change driven by loser elimination might therefore allow winner cells to spread with increasing their side number. This idea prompted us to investigate whether cell topology changes in the vicinity of apoptotic cells contribute to winner takeover during competition.

Using generalized mechanical simulations and *in vivo* imaging of *Drosophila* oncogenic clones, we show when and how winner cells selectively expand to compensate for local tissue volume loss after apoptosis of a loser cell. Following induction of locally overgrowing winners, slowly dividing normal cells adjacent to rapidly dividing winners show anisotropic distortion, as reported previously [25–28]. Immediately following apoptosis of the anisotropic normal cell, the space previously occupied by the apoptotic loser cell was filled by rapid cell expansion of adjacent winner cells. The winner cell expansion was unexpected, because previous studies mostly focused on cell division as the compensatory mechanism to fill space (e.g., "compensatory proliferation") [17, 29–32]. As a mechanism underlying this compensatory cell expansion of winners, we found that

This is an open access article under the CC BY license (http://creativecommons.org/licenses/by/4.0/).

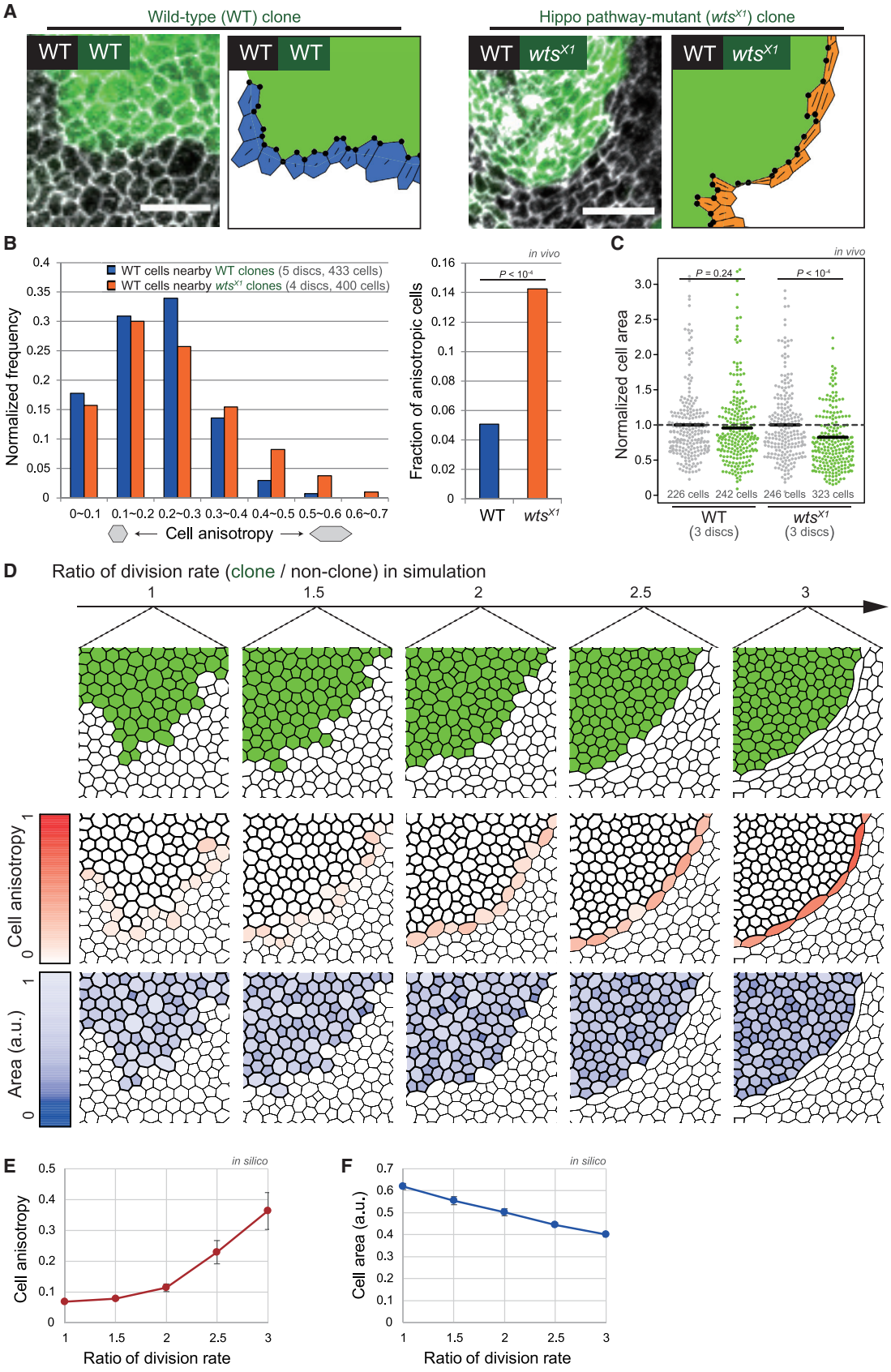

(legend on next page)

apoptosis of anisotropic losers adjacent to winners causes directionally biased cell intercalations, which re-establishes local cellular connectivity (cell topology) in a manner that selectively increases the apical surface area of winners. Importantly, such topological dynamics were verified with *in silico* and *in vivo* experiments in two different oncogenic genotypes (activated-Yki and Ras), where the overgrowing oncogenic population triggers apoptosis in surrounding wild-type cells. Furthermore, repetition of topological changes through the apoptosis of losers in immediate contact with winners, as observed in many cell competition systems [33], accelerates the tissue-scale expansion of winners *in silico*. Such rapid cell turnover via topological changes may disrupt tissue homeostasis to facilitate tumor initiation.

RESULTS

Differential Proliferation Induces Local Anisotropic Distortion in Slower Dividing Cells at the Clone Boundary and Compression in Faster Dividing Cells

To examine the cellular interaction during cell competition from a geometric perspective, we induced clones of GFP-expressing Hippo pathway mutant cells (winners; wts^{X1}) that rapidly proliferate and outcompete surrounding normal cells (losers; wild-type) in *Drosophila* wing discs [6]. Quantitative image analysis of apical cell shapes revealed two geometric alterations. First, wild-type cells directly adjacent to wts^{X1} clones showed significantly larger anisotropic distortions (Figure 1A, orange) than those directly adjacent to wild-type control clones (Figure 1A, blue and 1B; see STAR Methods for the fly strains and cell anisotropy definition), which was consistent with earlier reports [26, 27]. Second, the apical cell area of wts^{X1} clones was smaller than that of wild-type clones (Figure 1C), indicating that Hippo pathway mutant cells surrounded by wild-type cells are packed at a higher density.

We next examined whether the ectopic induction of over-proliferating cells was sufficient to cause these two geometric alterations (Figures 1B and 1C) in the vertex model. The vertex model is widely used to study mechanical deformation of multicellular tissue in response to cell bond tension and apical area contraction [22, 34–37] (Equation 1 in STAR Methods, Figures S1A and S1B). We introduced two clonal cell populations with different division rates into the model (Figures 1D and S1C). We confirmed anisotropic deformation of slower dividing cells localized at the clone boundary (Figures 1D, middle, 1E, and S1D), which is consistent with the wild-type cells directly adjacent to the wts^{X1} clone in the *Drosophila* experiment (Figure 1B) and earlier simulation studies [26, 28]. In addition, faster dividing cells were smaller than surrounding slower dividing cells (Figures 1D bottom, 1F, and S1E), similar to the wts^{X1} cells in the *Drosophila* experiment (Figure 1C). These results were consistent irrespective of different mechanical parameter values (Figures S1F and S1G) or formulations (another often used type Equation 2; Figures S2A–S2C). These deformations were never observed when two cell populations had identical division rates (Figure 1D, leftmost), and they were more apparent with greater differences in cell division rates (Figures 1E and 1F). These simulations suggest that differential proliferation rates are sufficient to reproduce two geometrical alterations in the *Drosophila* epithelium (Figures 1B and 1C).

We also examined the anisotropic cell deformation in the setting of differential tension between clonal and non-clonal cells since juxtaposition of wild-type and aberrant cells often affect junction mechanics [38, 39]. *In silico* experiments with all tension conditions showed that slower dividing cells at the clone boundary always exhibited higher anisotropy than those with identical proliferation rates (Figures S3A–S3C), demonstrating that differential tension does not have considerable influence on the cell anisotropy. Consistently, *in vivo* observation showed that the wild-type cell anisotropy beside clone was maintained even under modulation of junction contractility or adhesion in Hippo pathway mutant clones (Figures S1H and S1I). Collectively, these results suggest that localized over-proliferation induces anisotropic deformation in slower dividing cells at the clone boundary under differential tension.

Winner Cells Expand into Spaces Originally Occupied by Apoptotic Loser Cells with Higher Cell Anisotropy

Live imaging of cell competition was performed [7, 13, 16, 18, 20] in the *Drosophila* pupal notum to examine how space previously occupied by apoptotic loser cells is replaced. We induced faster dividing winner clones overexpressing an activated Yki ($UAS\text{-}yki^{S111A,S168A,S250A}\text{:}V5$; hereafter called Yki clones) [40], a transcriptional co-activator that acts downstream of the Hippo pathway (Figure 2A, left; Video S1). We observed that wild-type loser cells near Yki winner clones progressively took on anisotropic shapes (Figures 2A, right, and S1J), especially those between the Yki

Figure 1. Differential Proliferation Induces Local Anisotropic Distortion in Slower Dividing Cells at the Clone Boundary and Compression in Faster Dividing Cells

(A) Apical cell-cell junctions are marked by E-cad in the hinge region of *Drosophila* wing discs with representative clones: GFP-expressing cells are wild-type (WT clone, left) and wts^{X1} (wts^{X1} clone, left) cells, respectively, whereas non-GFP-expressing cells are wild-type cells (WT clone and wts^{X1} clone, left). Scale bar, 10 μm. Wild-type cells directly adjacent to the GFP-expressing clones were extracted, with black vertices representing tricellular junctions at the clone boundary and bars representing cell anisotropy (WT clone, right, blue and wts^{X1} clone, right, orange).

(B) Left: the distribution of cell anisotropy of wild-type cells directly adjacent to wild-type and wts^{X1} clones. Right: the fraction of cells whose anisotropy value is greater than 0.38. This threshold value was ranked in the top 5% of the value in the case inducing wild-type clones. Fisher's exact test was performed.

(C) Plot of apical area of non-GFP-expressing (gray) and GFP-expressing (green) cells at the clone boundary normalized to the average area of the non-GFP-expressing cells. Wilcoxon rank-sum test was performed.

(D) Top: closeup images of simulated clone at the indicated division rate ratios [clone (green) / non-clone (white)] when the number of clonal cells (green) is 1,000. Middle: anisotropy of non-clonal cells (top, white) along the clone boundary in the same field. Bottom: cell area of clonal cells (top, green) in the same field.

(E and F) Average anisotropy of non-clonal cells along the clone boundary (E) and average area of clonal cells directly adjacent to the clone boundary (F) were plotted as a function of the division rate ratio. Simulation setup is identical to (D). Error bars represent SD for 10 clones simulated at each division rate ratio. a.u., arbitrary unit.

See also Figures S1, S2, and S3.

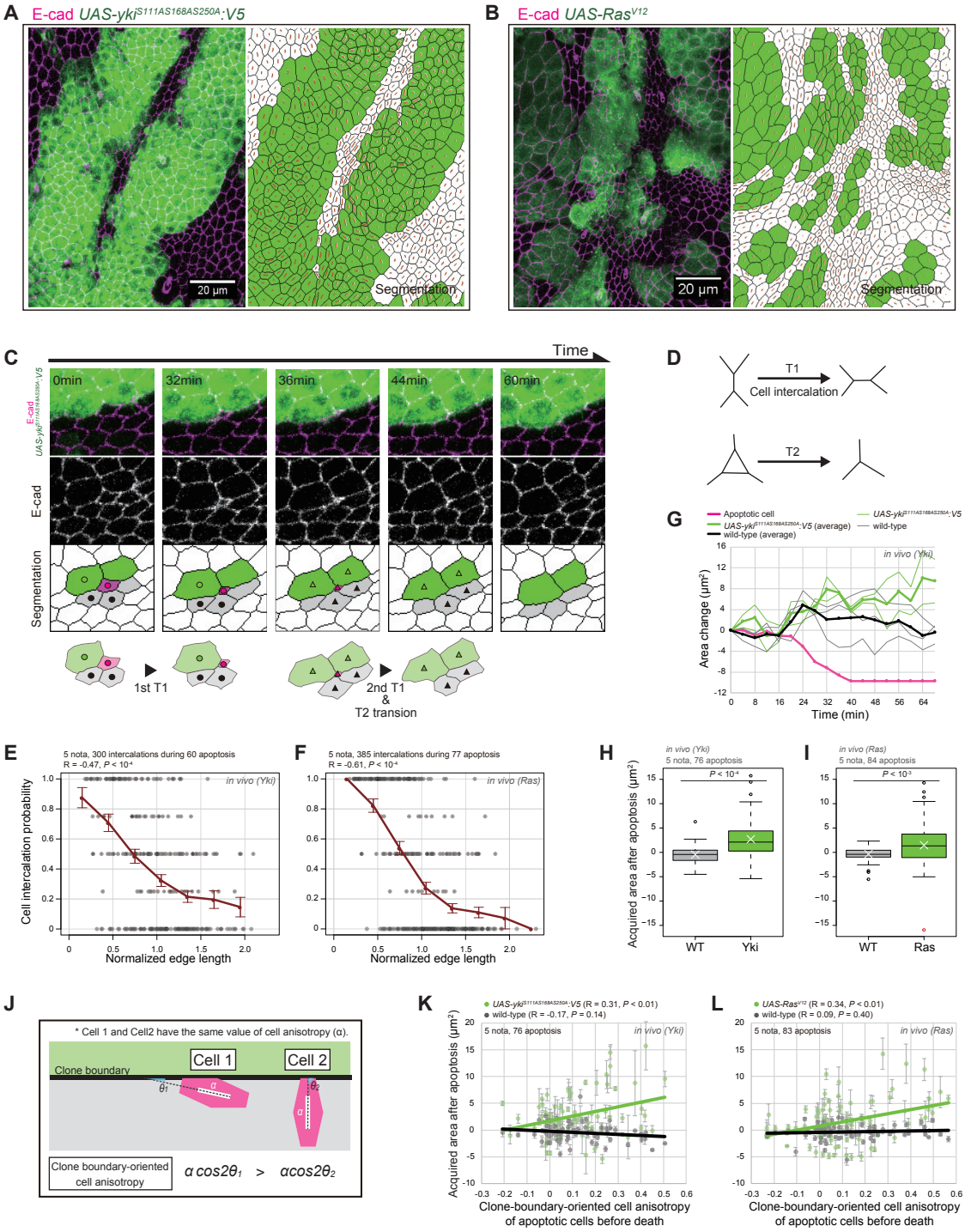

Figure 2. Winner Cells Expand into Spaces Originally Occupied by Apoptotic Loser Cells with Higher Cell Anisotropy in *Drosophila*

(A and B) Overexpression of Yki:V5^{S111A,S168A,S250A} (A) and Ras^{V12} (B). Left: Z projection of a snapshot (22.47 hr after Gal4-mediated transcription activation) taken during live imaging of pupal notum (anterior direction along the anterior-posterior axis is upward) with adherens junctions (indicated by E-cad::GFP; magenta) and clones (green). Right: image segmentation based on adherens junction localization shown in left panel. Strength and orientation of cell anisotropy [41] are indicated by brown.

(C) Time course of a loser delamination through repeated cell intercalations (known as D1-type delamination [7, 20]). Schematic drawings (lower panels) represents intercalations (open circle, filled circle, open triangle, filled triangle). Fly genotype is the same as in (A).

(D) Schematics of cell intercalation (T1 transition) and T2 transition.

(E and F) Cell intercalation probability as a function of edge length in dying cells 40 min before completion of apoptosis next to clones overexpressing Yki:V5^{S111A,S168A,S250A} (E) or Ras^{V12} (F). Each edge length was normalized to the averaged edge length of its belonging dying cell. Cell intercalation probability was

(legend continued on next page)

clones. Both anisotropic and isotropic loser cells were subsequently eliminated from the tissue (Figure S1J) by sequential cell intercalations from the shorter edges of a dying cell (Figures 2C–2E; Video S2). Although this elimination was observed at several cell diameters away from the clones, the majority of cell elimination occurred in cells immediately contact with Yki clones (Video S1). Upon repetitive loser elimination (apoptosis; see STAR Methods for the definition of "apoptosis" in this paper), Yki winner cells beside the clone boundary appeared progressively larger (Video S1). At the level of individual apoptosis, winner cells adjacent to apoptotic cells selectively replaced the space originally occupied by apoptotic loser cells through cell expansion; the area of faster dividing winner cells surrounding a dying cell increased, whereas the change in the area of slower dividing loser cells was negligible (Figures 2G and 2H). Another oncogenic winner-clone induced by an activated form of Ras (*UAS-Ras*^{V12}), which promotes cell growth and outcompetes surrounding wild-type cells in *Drosophila* [7, 42], also induced anisotropic distortion in wild-type cells at the clone boundary (Figures 2B and S1J). The Ras^{V12} winner cells expanded to compensate for wild-type loser cell apoptosis (Figures 2F and 2I). These results indicated that winner compensatory cell expansion was commonly observed upon induction of two oncogenic mutants, Yki and Ras^{V12}, which drive localized overgrowth through promoting proliferation or cell growth. The compensatory cell expansion of winners following apoptosis was unexpected considering the accepted hypothesis that lost territory is replaced as a result of winner-cell proliferation [29–32]. Moreover, we found that the winners' expansion was mediated by the anisotropic deformation of dying loser cells (Figure 1); the acquired area of Yki or Ras^{V12} winner cells positively correlated with anisotropy of dying loser cells (Figures S4A and S4J) that were oriented in parallel to the clone boundary (hereafter we call "clone-boundary-oriented anisotropy"; Figures 2J–2L and S4J).

We then applied a vertex model to determine whether winners used cell expansion to compensate for the volume lost after apoptosis of anisotropic loser cells. We incorporated apoptosis into the simulation based on the following experimental observations (Figure 2): (1) the target of apoptosis was slower dividing cells directly adjacent to faster dividing clones, (2) dying cell removal was induced by junctional loss due to sequentially introduced cell intercalations [7, 24] from the shorter edges of dying cells (Figure 3A; Video S3, see STAR Methods for apoptosis in simulations). Consistent with our previous experiments, the surrounding winner cells dominated expansion following apoptosis (Figure 3B). This winner-cell expansion was repeatedly observed in independent simulations that separately induced apoptosis in each individual loser cell at the clone boundary under differential proliferation rates, but it did not occur in the setting of identical proliferation rates (Figures 3C and S5A). This winner-cell expansion was consistently observed in several different model setups (formulation [Equation 2; Figure S2D], delamination process [Figures S3E–S3G], and differential tension conditions in clonal and non-clonal cells [Figure S3D]). Moreover, consistent with *in vivo* experiments, the rapidly dividing winner cells increasingly expanded as clone-boundary-oriented anisotropy of dying loser cells increased (Figures 3D, S2E, and S3H). We note that the rapid proliferation of winners in itself was not directly involved in the compensation process following apoptosis, because winner cells took over the territory of apoptosis despite ceasing all cell proliferation during the apoptotic simulation (Figure S3J). Therefore, we concluded that the emergent property under differential proliferation (i.e., local anisotropic distortion of apoptotic loser cells [Figure 1]), rather than differential proliferation in itself, has a key role in the compensatory expansion of winner cells.

Local Topological Change near Apoptosis Accompanies Winner-Dominated Cell Expansion

We then focused on cells immediately adjacent to an apoptotic cell to examine their contribution to winner-dominated cell expansion, because the territory lost to apoptosis was primarily occupied by the immediate neighbors, and cells located more than two cell distances away from the apoptotic cell acquired much smaller area (Figure S3I). We initially hypothesized that rapid winner-cell expansion was the result of a local compression difference between winner and loser cells surrounding the apoptosis (compression hypothesis; Figure 4A), because more compressed cells (Figures 1C and 1F) may generate stronger outward pushing forces that are enough to increase their cell area. To address this hypothesis, we tested whether compressed smaller cells adjacent to apoptosis were more likely to expand than larger cells. This hypothesis, however, seems not to be the case, because we observed that the cell area before apoptosis and their acquired area after apoptosis only correlated

determined whether intercalation occurred (probability = 1) or not (probability = 0) (see more details in Figures S4F–S4I). Each black point represents data calculated from a single cell intercalation event. Red dots represent binning of the averaged cell intercalation probability for every 0.3 normalized edge lengths. Error bars represent SE. R, Pearson correlation coefficient.

(G) Temporal change in cell area subtracted from value observed 40 min before delamination complete [Time = 0 (min)] was plotted for adjacent *UAS-yki*^{S111A,S168A,S250A}*:V5* (thin green line), wild-type cells (thin gray line) and an apoptotic cell (magenta line) in (C). The averaged acquired area is shown for faster (thick green line) and slower (thick black line) dividing cells.

(H and I) Boxplots of acquired area after apoptosis, which was obtained by averaging temporal change in cell area (G, thick lines) from 16 to 24 min after delamination complete, upon induction of clones overexpressing Yki:V5^{S111A,S168A,S250A} (H) or Ras^{V12} (I). The upper and lower hinges and middle line represent the 25th, 75th, and 50th percentiles, respectively. White Xs represent the averaged value. Wilcoxon signed-rank test was performed after excluding a dataset of outlier (a red dot in I) detected with the Smirnov-Grubbs test. All subsequent Ras^{V12} analyses were performed excluding the outlier dataset.

(J) Schematic of clone-boundary-oriented cell anisotropy (c; Equation 6 in STAR Methods), which considers both anisotropy strength (α; Equation 5) and its orientation relative to the clone boundary (θ).

(K and L) Acquired area after apoptosis (H and I) was plotted as a function of the clone-boundary-oriented anisotropy of apoptotic cells (Equation 6 in STAR Methods) 40 min before delamination completion and upon induction of clones overexpressing Yki:V5^{S111A,S168A,S250A} (K) or Ras^{V12} (L). Error bars represent SD for data collected 16–24 min after delamination completion. R, Pearson correlation coefficient.

See also Figures S1 and S4 and Videos S1 and S2.

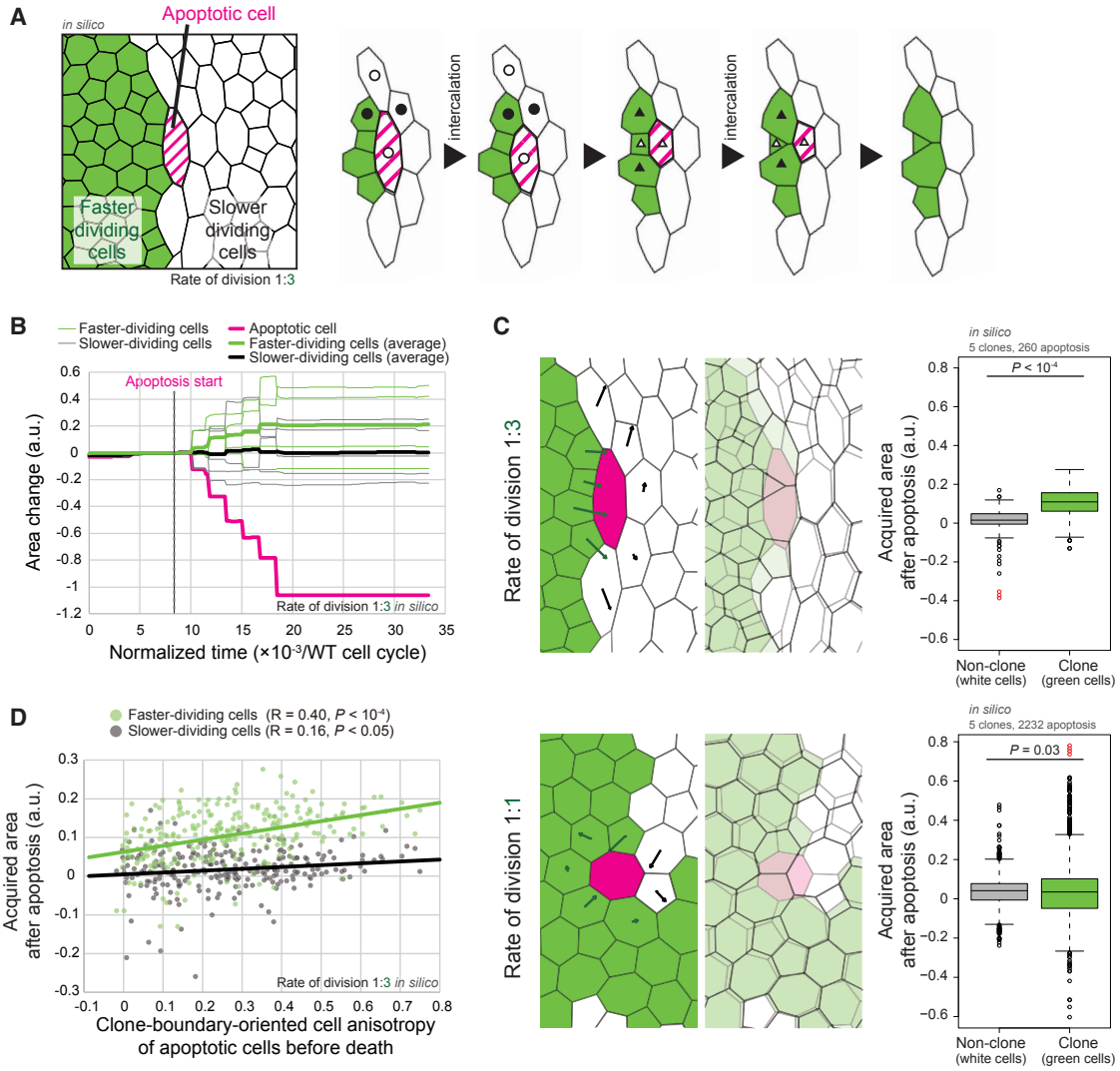

Figure 3. Winner Cells Expand into Spaces Originally Occupied by Apoptotic Loser Cells with Higher Cell Anisotropy in Simulations

(A) Time course of an apoptotic delamination with repeated cell intercalation (open circle, filled circle, open triangle, filled triangle). Apoptosis (magenta) was induced in a slower dividing cell (white) directly adjacent to the clone boundary when the number of faster dividing cells (green) was 1,000.

(B) Temporal change in cell area subtracted from pre-apoptosis value (normalized time [/loser cell cycle] = 8.3×10^{-3}) was plotted for adjacent faster (thin green line) and slower (thin gray line) dividing cells and an apoptotic cell (magenta line) in (A). The averaged acquired area for faster (thick green line) and slower (thick black line) dividing cells is shown. The step-like decreases in apoptotic cell area indicate six intercalation events.

(C) Differential (upper) and identical (lower) proliferation rates. Left: displacement of cells surrounding apoptotic cell at the time before and after apoptosis is shown by arrows; the ends of the arrows show the position of cell centroids at normalized time [/loser cell cycle] = 8.3×10^{-3} (tail end of arrow) and 2.5×10^{-2} (arrowhead). The displacement of clonal cells (green) was oriented toward the apoptotic cell (magenta) with differential proliferation rates (upper) and randomly oriented with identical proliferation rates (lower). Middle: overlay of pre- and post-apoptotic images at normalized time [/loser cell cycle] = 8.3×10^{-3} (light gray) and 2.5×10^{-2} (dark gray), respectively. Right: averaged acquired area (B, thick lines) after apoptosis completion (normalized time [/loser cell cycle] = 2.5×10^{-2}) when apoptosis was independently introduced into all non-clonal cells (white) directly adjacent to clone boundary. Wilcoxon signed-rank test was performed after excluding datasets of outliers (three and four red dots in upper and bottom panels, respectively) detected with the Smirnov-Grubbs test. Subsequent simulation analyses were performed excluding the outlier datasets.

(D) Averaged acquired area after apoptosis (C, right) plotted as a function of clone-boundary-oriented anisotropy (Equation 6 in STAR Methods) of apoptotic cells immediately before cell death (normalized time [/loser cell cycle] = 8.3×10^{-3}). As shape anisotropy of apoptotic cells increased, the winner-cell expansion became more pronounced. The division rate ratio (green/white) = 3 for (A, B, C, upper, D) and 1 for (C lower). R, Pearson correlation coefficient.

See also Figures S2, S3, and S5 and Video S3.

weakly, both *in silico* (Figure 4B) and in *in vivo* experiments with Yki and Ras^{V12} (Figures 4C and 4D). Additionally, in simulation, winner cells still took over the territory of apoptotic losers even if the tissue-scale pushing forces globally generated by release of winner-clone compression was suppressed during apoptosis by reducing the pressure parameter of all cells in winner clone (Figure S3J). These results suggested that local and global compression was insufficient to drive the process of rapid

compensatory expansion of winner cells, while winner compression was required for anisotropic deformation of loser cells (Figure 1).

As another hypothesis that locally mediates expansion, we focused on changes in local cellular connectivity (cell topology) driven by junctional remodeling (cell intercalation) upon apoptosis (Figures 2C and 3A). In epithelial cells in non-competitive tissue, there is a positive correlation between cell area and the side number representing local cellular connectivity (Lewis's law; Figure S1B) [22, 23, 43]. Based on this Lewis's law, an increase or decrease of side/edge number in each cell adjacent to apoptosis would be associated with cell area expansion or contraction (topology hypothesis; Figure 4E). We first confirmed that both winner (Yki or Ras^{V12}) and loser (wild-type) cells in competitive tissues obey this law (Figures 4I, 4J, S4D, and S4E), similar to non-competitive normal tissue. We then examined the topological changes following apoptosis and found that cells adjacent to apoptosis showed a strong positive correlation between the captured area and change in side number after apoptosis both *in silico* (Figure 4F) and in *in vivo* experiments with Yki and Ras^{V12} (Figures 4G and 4H). This suggests that cell intercalations during delamination lead to simultaneous increases in the side number and area of winner cells. These results prompted us to further test the topology hypothesis as a possible mechanism for winner-cell compensatory expansion.

Occurrence of Directionally Biased Cell Intercalation upon Apoptosis Correlates with Winner-Specific Increase in Cell Area

To understand how intercalations associated with apoptosis selectively increase winner side number and area, we first analyzed where cell intercalations took place relative to the clone boundary. Pupal notum junctions are reportedly subject to stochastic fluctuations of edge length that trigger cell intercalations by chance as edge lengths decrease to zero [44]. This framework suggests that shorter junctions are more likely to undergo intercalation, and our *in vivo* observations consistently showed a higher probability of intercalation at shorter edges (Figures 2E and 2F). In anisotropic dying cells caused by differential proliferation rates (Figure 1), edges perpendicular to the clone boundary were shorter than other edge types (Figures 5A–5C, S4B, and S5B; see Figure 5D for edge classification), suggesting that these perpendicular edges were more likely to be eliminated by cell intercalation. Indeed, both *in silico* and *in vivo* experiments with Yki and Ras^{V12} indicated that cell intercalation likely occurred in a manner to eliminate the perpendicular edges (perpendicular intercalation) during anisotropic loser cell delamination (Figures 5F–5H, S2F, S4C, and S5C; see Figures 5D, 5E, and S4F–S4I for the definition of normalized frequency of cell intercalation). Moreover, the increased frequency of perpendicular intercalation during an apoptotic event increased the side number and area of winner cells after apoptosis, but not that of loser cells (Figures 5O–5Q, S2I, S4M, and S5F). We did not observe this effect for the two other types of intercalation that occurred at boundary and non-boundary edges (Figures 5I–5N, S2G, S2H, S4K, S4L, S5D, and S5E). Thus, perpendicular intercalation frequency during each apoptosis event uniquely correlates with selective increases in winner side number and occupied area.

Perpendicular Intercalation Directly Drives Winner-Compensatory Cell Expansion

We next asked how the perpendicular intercalation selectively drives winner-cell expansion. Of the four cells involved in intercalation upon apoptosis (one dying cell and three surviving cells; Figure 6A, upper), two surviving cells gain a single side, whereas the other surviving cell and the dying cell each lose a side after an intercalation event. Based on this rule, we comprehensively calculated topology changes (side number) in winner and loser cells for all geometrically possible intercalations (Figure 6A, table). For example, in a subtype of perpendicular intercalation (second row from bottom of table in Figure 6A), a winner cell increases side number by one, whereas each of two loser cells increases or decreases by one, respectively, and therefore these two cancel out the change in side number of losers in total. Notably, all the subtypes of perpendicular intercalation uniquely increase winner-cell side number and area in total, whereas those of boundary and non-boundary intercalations mainly increase for loser cells in total (Figure 6A, table). *In silico* experiments were performed to determine whether perpendicular intercalation is sufficient to drive winner-dominated cell expansion. In the simulation, we introduced a directionally biased event of boundary, non-boundary, or perpendicular intercalation upon apoptosis under identical proliferation conditions (Figures 6B and S5I) where intercalation is typically unbiased (Figures S5G and S5H). This allowed us to examine the contribution of directionally biased intercalation to winner-cell expansion (topology hypothesis; Figure 4E) in the absence of winner compression (compression hypothesis; Figure 4A). By introduction of biased perpendicular intercalation during apoptosis, clonal cells directly in contact with apoptosis consistently increased both their side number and area averaged for each apoptotic event, whereas non-clonal cells in direct contact with apoptosis did not (Figure 6B, right). In contrast, neither side number nor area of clonal cells increased upon the prioritized induction of boundary and non-boundary intercalations (Figure 6B, left and middle). This indicates that frequent perpendicular intercalation upon apoptosis directly increases side number and area in winner cells.

Repetitive Topological Change by Perpendicular Intercalation Accelerates Tissue-Scale Occupation by Winners

Finally, we examined the long-term topological change upon sequential induction of apoptosis in multiple loser cells at clone boundaries (Figure 7A). After simulating repetitive apoptosis where intercalations occur from shorter edges according to *in vivo* regular rule as shown in Figures 2E and 2F, winner clones took over almost 100% of the total cell area that was lost to apoptosis (Figure 7D, purple), and consequently, winner cells spread more rapidly than in the absence of apoptosis (middle and left panels of Figure 7B and Video S4; Figure 7C, purple and black). This long-term expansion of winner cells was ensured by stably maintaining anisotropy of loser cells during multiple apoptosis events (Figure 7E) in which loser cells that were newly faced with clone boundaries after apoptosis subsequently became anisotropic (Figure S6). Due to the maintenance of a high-degree of cell anisotropy, the frequency of perpendicular intercalation remained high during apoptosis (Figure 7F). This allowed winner cells at the outermost layer of the clone

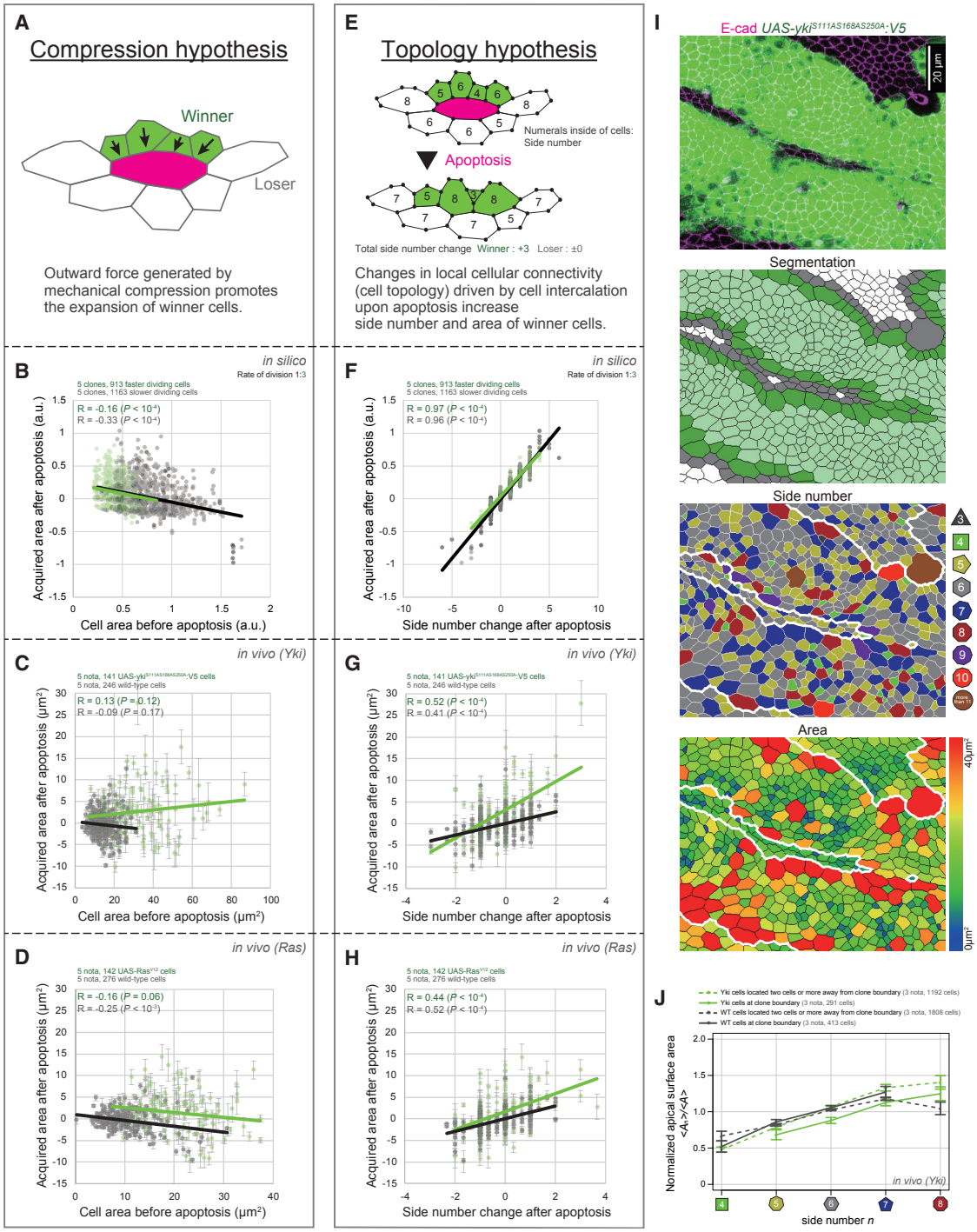

Figure 4. Two Hypothetical Mechanisms of Winner-Dominated Cell Expansion

(A) Compression hypothesis. Compressed, faster dividing winner cells (green) should occupy the space left by the apoptotic cells (magenta) because the apical area of these compressed cells is smaller than their preferred area. Therefore, the winner cells (green) are more likely than the non-compressed loser cells (white) to expand when space becomes available.

(B–D) Compression hypothesis testing (A). Area acquired by individual surviving cells directly in contact with apoptotic cells as a function of initial pre-apoptotic area of the surviving cells, which reflects degree of mechanical compression. The pre-apoptotic area was measured at a normalized time [/loser cell cycle] = 8.3×10^{-3} *in silico* (B) and 40 min before apoptosis completion *in vivo* (Yki:V5^{S111A,S168A,S250A}, C; Ras^{V12}, D). Temporal average of the acquired areas of cells directly in contact with apoptosis and SD (error bars) *in vivo* were calculated 16–24 min after apoptosis completion. See the definition of acquired area for Figures 2G or 3B (thin lines). R, Pearson correlation coefficient.

(legend continued on next page)

persistently increased their side number and area for a long-term during clone development (Figures S7A–S7C). Additionally, winner cells inside clones (i.e., more than two cell distances away from the clone boundary) also slightly expanded on a longer timescale (Figure S7E, inside) without changing side number (Figure S7D, inside), possibly due to an accumulation of minor relaxations of mechanical compression (Figure S3I, acquired area of winner cells localized to two- or three cells away from apoptotic cells). We note that this increase in cell area by mechanical relaxation was relatively modest compared to the dramatic area expansion as a result of cell topological change at the clone border (Figures S7D and S7E). These results suggest that topological change driven by frequent perpendicular intercalation is still critical for long-term winner-clone spreading. Accordingly, we incorporated random directionality into intercalations associated with apoptosis under differential proliferation rates to assess whether winner-clone spreading is disrupted by the unbiased occurrence of three intercalation types (randomized intercalation; right panels of Figure 7B; Video S4). We found that clone spreading speed was reduced (Figure 7C, light-blue) due to equal and simultaneous increases in the side number and cell area of both winner and loser cells (Figures S7B and S7C, bottom panel). As such, the net increase in winner-clone area after loser apoptosis was reduced to approximately 50% of the total area lost to apoptosis (Figure 7D, light blue), confirming that topological change at the clone boundary significantly contributed to winner-clone spreading.

Because topological change due to apoptosis is limited to cells in direct contact with apoptotic cells, loser death restricted nearby winner clones, as seen in many cell competition systems [33], would promote winner-clone spreading. We examined *in silico* whether the restricted death actually improves winner expansion by comparing it to a scenario in which apoptotic cells were spatially scattered in slower dividing cell population. We found winner clones most effectively occupied the apoptotic territory when loser apoptosis was restricted to the clone boundary (Figures S7F–S7H, up to 1-cell distance). On the other hand, occupation efficiency was reduced when apoptosis had a more scattered spatial distribution (Figures S7F–S7H, up to 3- or 5-cell distance) and further dropped down to baseline (no apoptosis) when death had a completely random distribution (Figures S7F–S7H, all slower dividing cells). Collectively, we can conclude that repetitive cell topology changes due to frequent perpendicular intercalation at the clone periphery accelerates tissue-scale occupation by winner cells.

DISCUSSION

It has long been acknowledged that loser apoptosis is limited to within several cell diameters away from winner clones in many cell competition systems [33]. However, it was unclear how this localized apoptosis influences subsequent winner tissue occupation. Here, we showed that localized apoptosis adjacent to the clone boundary efficiently accelerates winner-clone expansion through cell topological changes, indicating that regulating topology might have a major contribution to tissue takeover by winners (Figures 7 and S7). We also identified the mechanisms underlying these topological alterations (Figure 7G): anisotropic loser cells driven by localized overgrowth (Figures 1, 2A, and 2B) undergo apoptosis, producing a non-cell-autonomous increase in the side numbers and areas of surrounding winner cells (Figures 2 and 3). This topological alteration was verified with *in silico* and *in vivo* experiments in two different oncogenic genotypes (activated-Yki and Ras), which targets different signaling pathways but commonly show overgrowth phenotype. These results indicate their common feature, differential growth, may be the origin of the topological dynamics leading to winner-cell expansion, while Yki can be activated by Ras signaling [45, 46] and winner-cell expansion may be driven at least in part through Yki activation.

We further showed *in silico and in vivo* that such topological dynamics leading to selective winner expansion is regulated by directionally biased cell intercalation (Figures 5 and 6), which occurs as a consequence of perpendicular edge shortening in anisotropic apoptotic cells (Figures 2E, 2F, and 5A–5C). Although polarized actomyosin-dependent mechanical tension is well known to bias intercalation direction in many morphogenetic processes [47, 48], the Hippo pathway mutant clone in the *Drosophila* epithelium did not accumulate myosin II or increase tension at the radial junction (i.e., perpendicular edge) but did at the circumferential junction (i.e., non-boundary edge) of wild-type cells surrounding clones [26, 27]. The compensatory expansion of winner cells upon apoptosis should therefore be achieved by stochastic junction loss at the shorter perpendicular edges rather than greater tension due to active myosin enrichment.

(E) Topology hypothesis. Topological changes driven by repetitive cell intercalations upon apoptosis (magenta) should selectively increase in side number and area of winner cells.

(F–H) Topology hypothesis testing (E). Area acquired by individual surviving cells directly in contact with apoptotic cells as a function of side number change, which was calculated by subtracting the initial side number {normalized time [/loser cell cycle] = 8.3×10^{-3} *in silico* (F), 40 min before apoptosis completion *in vivo* [Yki:V5^{S111A,S168A,S250A} (G), Ras^{V12} (H)]} from the final side number {normalized time [/loser cell cycle] = 2.5×10^{-2} *in silico* (F), average for 16–24 min after apoptosis completion *in vivo* (G and H)}. The y axis value is the same as that in (B)–(D). R, Pearson correlation coefficient.

(I) Top: Z projection of a live pupal notum upon induction of clones overexpressing Yki:V5^{S111A,S168A,S250A} (25 hr after Gal4-mediated transcription activation). Fly genotype and image frame is the same as in Figure 2A; the anterior direction is leftward. Second panel from top: image segmentation for adherens junctions shown in top panel. Green and gray cells represent Yki-overexpressing and wild-type cells at clone boundary, whereas light green and white cells represent Yki-overexpressing and wild-type cells located two cell distances or more away from clone boundary. Side number (third from top) and area (bottom panel) of each cell are indicated by colors. White thick line represents clone boundary.

(J) Averaged area of cells with n-sides (A_n) normalized by that of all cells for each cell category (A) (i.e., A_n/A where < > denotes the population average) at 25–26 hr after Gal4-mediated transcription activation. Cells were classified into four categories: green and gray solid lines are Yki-overexpressing and wild-type cells, respectively, at the clone boundary (green and gray cells in I, second panel), whereas green and gray broken lines are Yki-overexpressing and wild-type cells, respectively, located at a distance of two cells or more away from the clone boundary (light green and white cells in I, second panel). Error bars represent SE. See also Figures S1, S3, and S4 and Video S1.

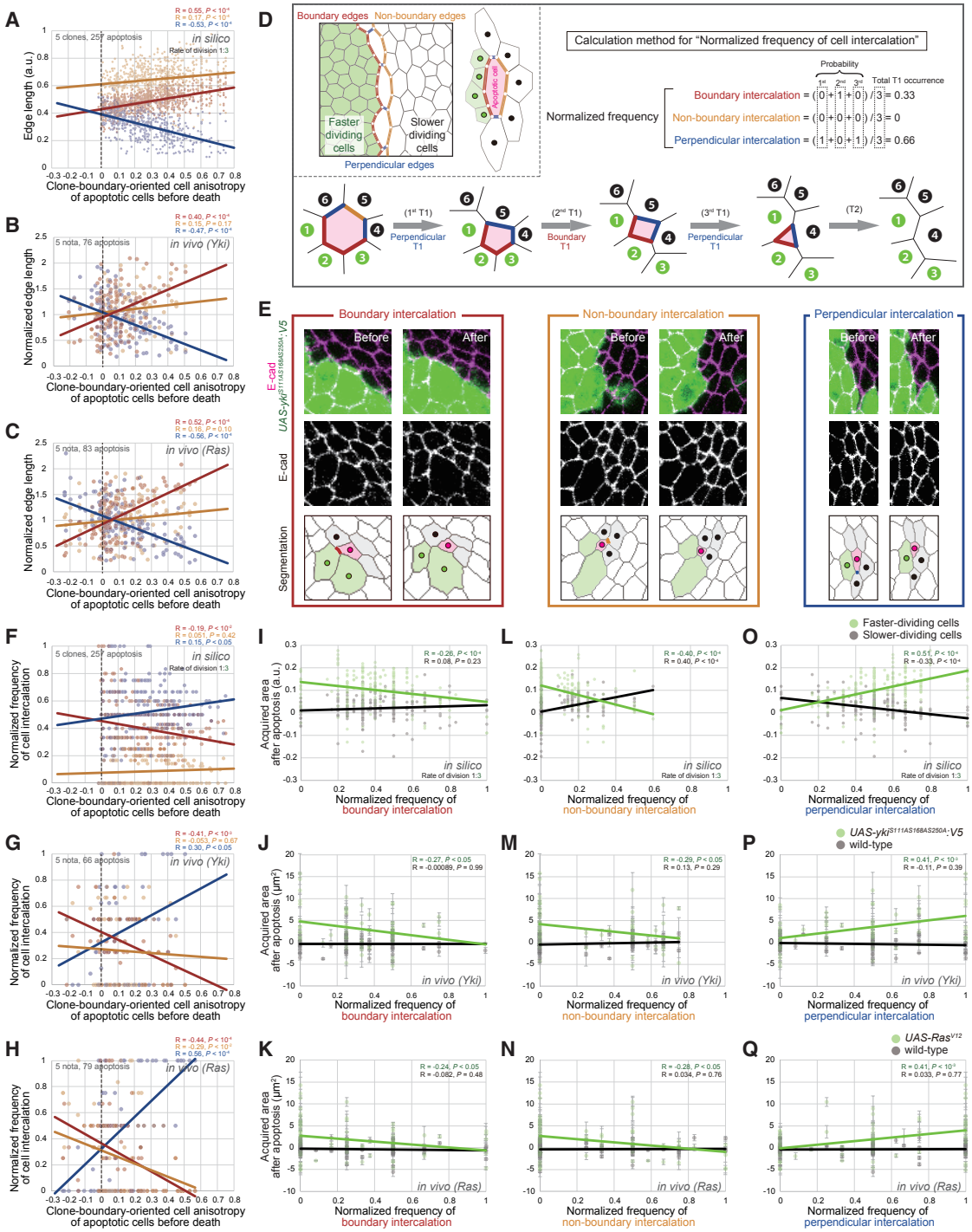

Figure 5. Occurrence of Directionally Biased Cell Intercalation upon Apoptosis Correlates with Winner-Specific Increase in Cell Area

(A–C) The length distribution of three types of edges introduced in (D) (inset) as a function of clone-boundary-oriented anisotropy (Equation 6 in STAR Methods) of an apoptotic cell before death. The x axis values are the same as that in Figure 3D for simulation and in Figures 2K and 2L for experiments. The y axis values of experiment (Yki:V5^{S111A,S168A,S250A}, B; Ras^{V12}, C) are the same as those in the x axis of Figures 2E and 2F. R, Pearson correlation coefficient.

(D) A calculation example for the "normalized frequency of cell intercalation" for each type used in (F)–(Q). Green circled numbers 1–3 indicate clonal cells, whereas black circled numbers 4–6 indicate non-clonal cells. The normalized frequency was calculated by dividing the sum of the probability of each intercalation event by the total number of intercalation events. The classification of edges was determined each time after an intercalation. Inset: classification of edges belonging to apoptotic loser cells (right, magenta cell). Boundary edge (red): edges on the clone boundary. Non-boundary edge (orange): edges between the two vertices, neither of which are at the clone boundary. Perpendicular edge (blue): edges located perpendicular to clone boundary.

(legend continued on next page)

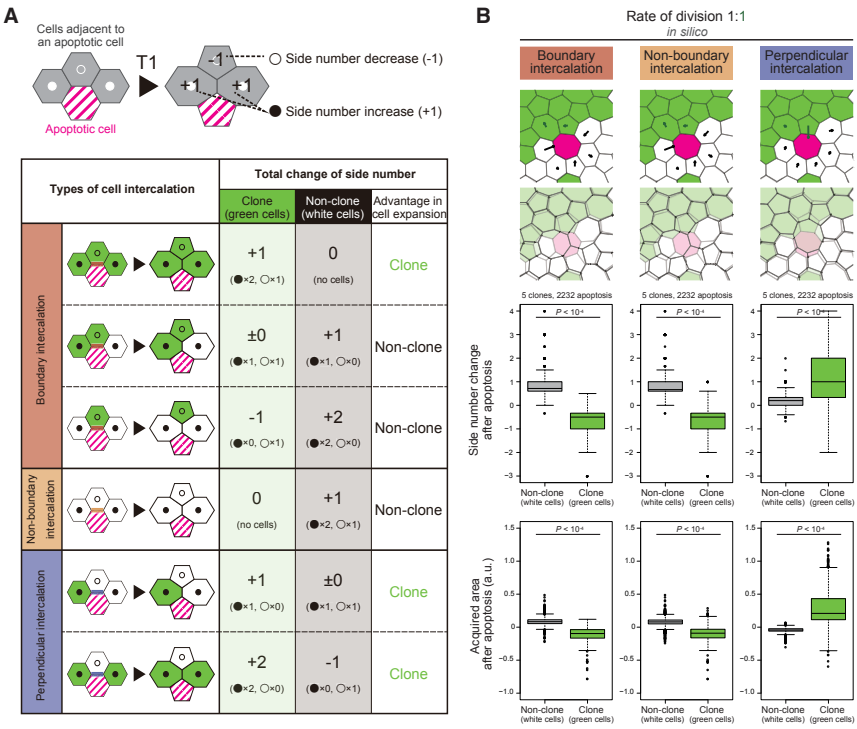

Figure 6. Perpendicular Intercalation Directly Drives Winner-Compensatory Cell Expansion

(A) Upper: schematic diagram of the topological changes in three cells directly in contact with the apoptotic cell (magenta) that are directly involved in cell intercalation during apoptosis (Figure 3A). After intercalation, side number is reduced by one for one adjacent cell (−1, open circles), but is increased by one for the other two cells (+1, filled circles). Lower: three types of cell intercalation (Figure 5E) were divided into six subtypes based on all possible combinations of cell configuration. Total change in side number after intercalation is shown for clonal (green columns) and non-clonal (gray columns) cells. Advantage in cell expansion represents cells with a greater increase in total side number. All topological changes are maintained whenever side number of apoptotic cell is more than 4 before apoptosis.

(B) Top, schematic representation of the indicated intercalation types. Lower boxplots, change in side number (upper boxplots) and cell area (bottom boxplots) averaged for each apoptotic event. Apoptotic simulation was performed with a predetermined order of directionally biased cell intercalation under identical division rate conditions. The simulation setup (except for the directional bias in intercalation) and figure preparation were the same as for Figure 3C lower. Wilcoxon signed-rank test was performed.

See also Figure S5.

In addition to perpendicular intercalation, our theoretical analysis indicates that a specific boundary intercalation subtype increases winner-cell side number and area following apoptosis (top row of table in Figure 6A). Because the subtype only occurs when all surviving cells involved in the intercalation were winners, it should be frequent when an apoptotic cell shares more sides with winner cells. This situation in which the boundary intercalation subtype is more frequent than perpendicular intercalation might be rare in Yki- or Ras-activating clones with fewer shared sides due to cell sorting [38], but frequent in Myc- or minute-dependent competition, where winner and loser cells actively mix to increase their shared sides [17, 20, 49]. Moreover, regarding the expansion process, intercalation-mediated space filling does not require cell division (Figure S3J). This fact is supported by live notum imaging that shows winner expansion even after growth arrest (approximately after time = 28.5 in Video S1). Therefore, intercalation-mediated winner expansion might contribute to the competition scenario without proliferation (e.g., post-mitotic tissue [50]). Future examination of the relative contributions of intercalation subtypes in various cell competition scenarios would clarify the topological dynamics that lead to selective winner expansion.

Given the knowledge that a striking increase in cell apical area stimulates proliferation through feedback regulation by mechanical signaling pathways in non-competitive tissue [51, 52], we expected that the dramatic increase in winner-cell area that follows loser apoptosis (Figure 7) would facilitate winner proliferation. As such, the increase in cell area by topological change is transformed into the increase in cell number, which could further accelerate long-term clone expansion. It was recently suggested that mechanical or morphological consequences of cell loss affect the division orientation of winner cells, which colonize lost territory [17, 49]. Therefore, examination of the contribution of positive feedback on winner division rate and orientation *in silico* [36] and *in vivo* would provide a more comprehensive understanding of winner-clone spreading. Although it was difficult to detect this positive feedback effect on cell division with our live imaging in notum, due to growth arrest during terminal

(E) Examples of three types of cell intercalation, which are classified according to the types of disappearing edges (D, inset), in pupal notum. Fly genotypes are the same as in Figure 2A.

(F–H) Normalized frequency of three intercalation types observed in a single apoptosis event as a function of anisotropy of an apoptotic cell before death (Equation 6 in STAR Methods). The x axis values for simulation (F) and experiment (Yki:V5^{S111A,S168A,S250A}, G; Ras^{V12}, H) are the same as in (A)–(C). R, Pearson correlation coefficient.

(I–Q) Averaged acquired area of winner cells (green) and loser cells (gray) as a function of normalized frequency of boundary (I–K), non-boundary (L–N), and perpendicular (O–Q) intercalation in simulations (I, L, and O) and experiments (Yki:V5^{S111A,S168A,S250A}, J, M, and P; Ras^{V12}, K, N, and Q). The x axis values are the same as the y axis (F) for simulations and in (G) and (H) for experiments, whereas the value and error bars in the y axis corresponds to y axis in Figure 3D for simulation and a subset of Figures 2K and 2L for experiment. R, Pearson correlation coefficient.

See also Figures S2, S3, S4, and S5.

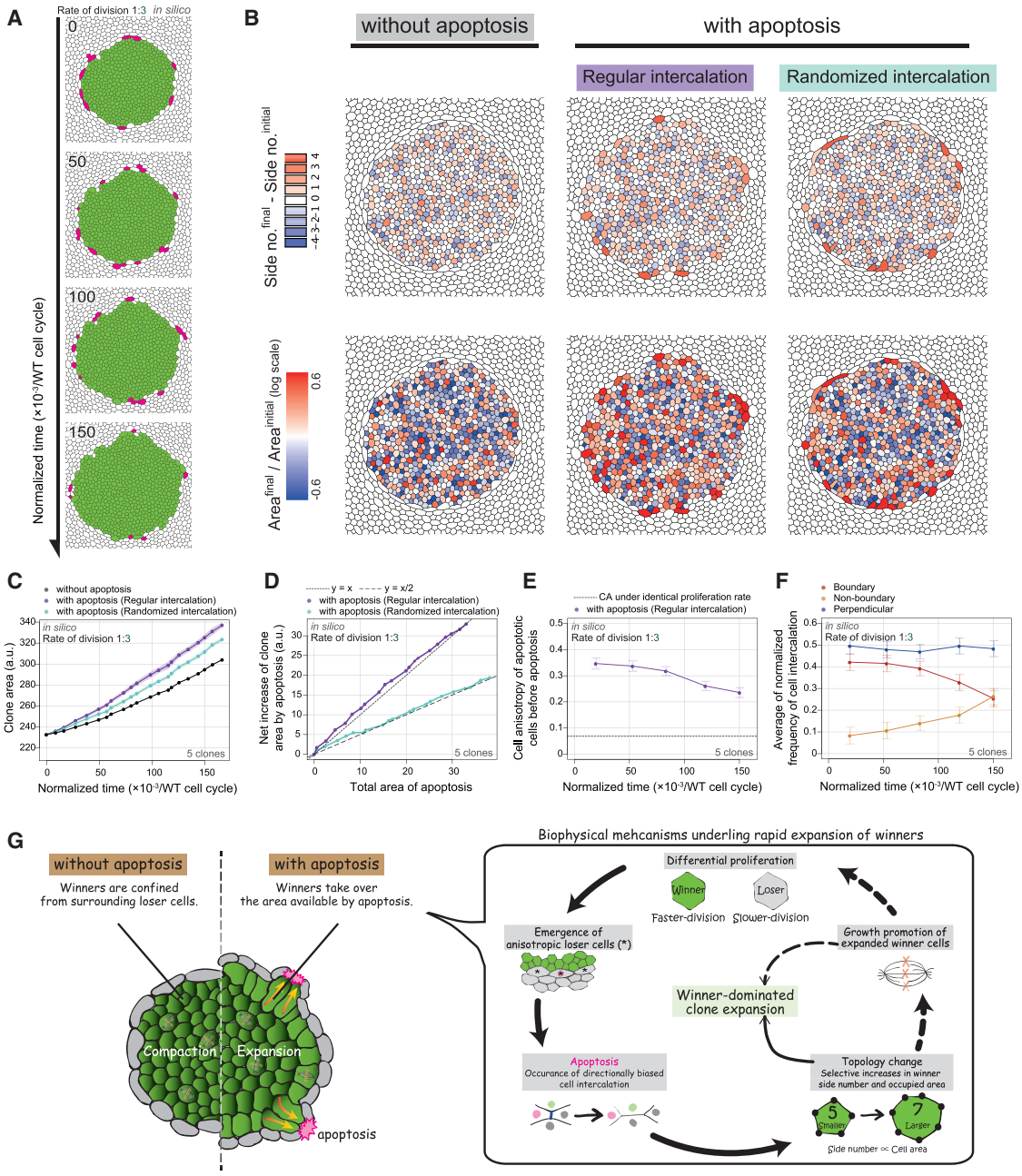

Figure 7. Repetitive Topological Change by Perpendicular Intercalation Accelerates Tissue-Scale Occupation by Winners

(A) Loser cells that will start to undergo apoptosis within the next 50 (normalized time [/loser cell cycle]) are shown in magenta. Apoptosis was induced in about 40 cells adjacent to winners while the number of faster dividing winner cells (N_{faster}, green) increased from 500 to 700 cells.

(B) Closeup of colored winner-clone when N_{faster} is 700. Change in side number is shown by subtracting initial (N_{faster} = 500) from final (N_{faster} = 700) side number (upper 3 panels). The log of the ratio of the final cell area over initial cell area is shown (lower 3 panels). Simulation setups were without apoptosis (left); with apoptosis where intercalations occur from shorter edges according to *in vivo* regular rule as shown in Figures 2E and 2F (middle; regular intercalation); and with apoptosis where three intercalation types occur randomly (right; randomized intercalation). The number of winner-cell divisions and initial clone (A, normalized time = 0 [/loser cell cycle]) were the same for the three simulation setups.

(C) Temporal change in clone area with no apoptosis (black), apoptosis with regular intercalation (purple) and apoptosis with randomized intercalation (light-blue). Error bars represent SD.

(D) Net increase in clone area as a result of apoptosis calculated by subtracting clone area from that value in the absence of apoptosis as a function of total area of apoptosis. Dashed/dotted lines indicate cases in which winner clones capture 50%/100% of the territory made available by apoptosis.

(E) Temporal change in anisotropy of apoptotic cells (measured at 1.7×10^{-3} normalized time [/loser cell cycle] before starting to undergo apoptosis). The values were clearly larger than those under conditions of identical proliferation rate without apoptosis (dashed line). Error bars represent SE.

(legend continued on next page)

differentiation, it will be interesting to monitor the contribution of cell expansion to division in actively growing tissue.

STAR★METHODS

Detailed methods are provided in the online version of this paper and include the following:

- KEY RESOURCES TABLE
- CONTACT FOR REAGENT AND RESOURCE SHARING
- EXPERIMENTAL MODEL AND SUBJECT DETAILS
  - *Drosophila* strains and genetics
  - Experimental genotypes
  - Husbandry conditions
- METHOD DETAILS
  - Immunohistochemistry and fixed-sample imaging
  - Live imaging of pupal notum
  - Vertex model
- QUANTIFICATION AND STATISTICAL ANALYSIS
  - Calculation of cell shape anisotropy
  - Cell area and shape in fixed-sample imaging
  - Image segmentation
  - Apoptosis analysis in live imaging
  - Cell shape, topology, and apoptosis in live imaging
  - Statistical analysis

SUPPLEMENTAL INFORMATION

Supplemental Information includes seven figures and four videos and can be found with this article online at https://doi.org/10.1016/j.cub.2018.05.029.

ACKNOWLEDGMENTS

We thank T. Kondo, K. Hironaka, M.S. Kitazawa, and K. Matsushita for valuable comments on the manuscript draft; Y. Fujita, S. Hayashi, S. Ishihara, and K. Sugimura for discussions; K. Matsuno for technical support; K. Ikeguchi, Y. Matsumoto, M. Hirohata, M. Kishino, and M. Kobayashi for the segmentation of experimental images; T. Xu, D.J. Pan, Bloomington Stock Center, and Vienna Drosophila Resource Center for fly stocks; and B. Aigouy for the tissue analyzer. A.T. is a JSPS Research Fellow (15J01837). This work supported by Grants-in-Aid for Scientific Research from MEXT to S.O. (15H05862, 17H03673), D.U. (15K18536, 17K07402, 17H02939), E.K. (JP26114003, JP16H04800, 17K19884), T.I. (26114002, 16K14606, 16H02505), and K.F. (15H01490, 17H05619, 17H06386).

AUTHOR CONTRIBUTIONS

A.T., S.O., D.U., E.K., T.I., and K.F. designed the study. S.O. and T.I. designed fixed tissue imaging experiments. D.U. and E.K. designed live imaging experiments. S.O., Y.S., and A.T. performed fixed tissue imaging. A.T. performed cell image analysis and computer simulations. A.T. and D.U. performed live imaging and developed methods and scripts for data analysis. All authors discussed the results. A.T., K.F., T.I., D.U., and S.O. wrote the paper.

DECLARATION OF INTERESTS

The authors declare no competing interests.

Received: November 3, 2017
Revised: April 9, 2018
Accepted: May 11, 2018
Published: June 14, 2018

REFERENCES

1. Eichenlaub, T., Cohen, S.M., and Herranz, H. (2016). Cell competition drives the formation of metastatic tumors in a Drosophila model of epithelial tumor formation. Curr. Biol. *26*, 419–427.
2. Suijkerbuijk, S.J.E., Kolahgar, G., Kucinski, I., and Piddini, E. (2016). Cell competition drives the growth of intestinal adenomas in Drosophila. Curr. Biol. *26*, 428–438.
3. Johnston, L.A., Prober, D.A., Edgar, B.A., Eisenman, R.N., and Gallant, P. (1999). Drosophila myc regulates cellular growth during development. Cell *98*, 779–790.
4. de la Cova, C., Abril, M., Bellosta, P., Gallant, P., and Johnston, L.A. (2004). Drosophila myc regulates organ size by inducing cell competition. Cell *117*, 107–116.
5. Moreno, E., and Basler, K. (2004). dMyc transforms cells into super-competitors. Cell *117*, 117–129.
6. Tyler, D.M., Li, W., Zhuo, N., Pellock, B., and Baker, N.E. (2007). Genes affecting cell competition in Drosophila. Genetics *175*, 643–657.
7. Levayer, R., Dupont, C., and Moreno, E. (2016). Tissue crowding induces caspase-dependent competition for space. Curr. Biol. *26*, 670–677.
8. Li, W., and Baker, N.E. (2007). Engulfment is required for cell competition. Cell *129*, 1215–1225.
9. Martín, F.A., Herrera, S.C., and Morata, G. (2009). Cell competition, growth and size control in the Drosophila wing imaginal disc. Development *136*, 3747–3756.
10. Simpson, P. (1979). Parameters of cell competition in the compartments of the wing disc of Drosophila. Dev. Biol. *69*, 182–193.
11. Simpson, P., and Morata, G. (1981). Differential mitotic rates and patterns of growth in compartments in the Drosophila wing. Dev. Biol. *85*, 299–308.
12. Igaki, T., Pastor-Pareja, J.C., Aonuma, H., Miura, M., and Xu, T. (2009). Intrinsic tumor suppression and epithelial maintenance by endocytic activation of Eiger/TNF signaling in Drosophila. Dev. Cell *16*, 458–465.
13. Ohsawa, S., Sugimura, K., Takino, K., Xu, T., Miyawaki, A., and Igaki, T. (2011). Elimination of oncogenic neighbors by JNK-mediated engulfment in Drosophila. Dev. Cell *20*, 315–328.
14. Wagstaff, L., Goschorska, M., Kozyrska, K., Duclos, G., Kucinski, I., Chessel, A., Hampton-O'Neil, L., Bradshaw, C.R., Allen, G.E., Rawlins, E.L., et al. (2016). Mechanical cell competition kills cells via induction of lethal p53 levels. Nat. Commun. *7*, 11373.
15. Yamamoto, M., Ohsawa, S., Kunimasa, K., and Igaki, T. (2017). The ligand Sas and its receptor PTP10D drive tumour-suppressive cell competition. Nature *542*, 246–250.
16. Bove, A., Gradeci, D., Fujita, Y., Banerjee, S., Charras, G., and Lowe, A.R. (2017). Local cellular neighbourhood controls proliferation in cell competition. Mol. Biol. Cell *28*, 3215–3228.
17. Li, W., Kale, A., and Baker, N.E. (2009). Oriented cell division as a response to cell death and cell competition. Curr. Biol. *19*, 1821–1826.
18. Kajita, M., Sugimura, K., Ohoka, A., Burden, J., Suganuma, H., Ikegawa, M., Shimada, T., Kitamura, T., Shindoh, M., Ishikawa, S., et al. (2014). Filamin acts as a key regulator in epithelial defence against transformed cells. Nat. Commun. *5*, 4428.

(F) Temporal change in normalized frequencies of three types of cell intercalation (see calculation method in Figures 5D and S4F–S4I), which were averaged for every 33.3×10^{-3} (normalized time [/loser cell cycle]). Error bars represent SE. Division rate ratio (green/white) = 3 for all panels.
(G) Schematic diagram of the winner-dominated expansion toward the space of apoptosis. Inset: solid lines are based on our findings, whereas dashed lines represent speculation suggested in previous reports.
See also Figures S3, S6, and S7 and Video S4.

19. Clavería, C., Giovinazzo, G., Sierra, R., and Torres, M. (2013). Myc-driven endogenous cell competition in the early mammalian embryo. Nature *500*, 39–44.

20. Levayer, R., Hauert, B., and Moreno, E. (2015). Cell mixing induced by myc is required for competitive tissue invasion and destruction. Nature *524*, 476–480.

21. Gibson, M.C., Patel, A.B., Nagpal, R., and Perrimon, N. (2006). The emergence of geometric order in proliferating metazoan epithelia. Nature *442*, 1038–1041.

22. Farhadifar, R., Röper, J.-C., Aigouy, B., Eaton, S., and Jülicher, F. (2007). The influence of cell mechanics, cell-cell interactions, and proliferation on epithelial packing. Curr. Biol. *17*, 2095–2104.

23. Lewis, F.T. (1928). The correlation between cell division and the shapes and sizes of prismatic cells in the epidermis of cucumis. Anat. Rec. *38*, 341–376.

24. Marinari, E., Mehonic, A., Curran, S., Gale, J., Duke, T., and Baum, B. (2012). Live-cell delamination counterbalances epithelial growth to limit tissue overcrowding. Nature *484*, 542–545.

25. Vincent, J.-P., Fletcher, A.G., and Baena-Lopez, L.A. (2013). Mechanisms and mechanics of cell competition in epithelia. Nat. Rev. Mol. Cell Biol. *14*, 581–591.

26. Mao, Y., Tournier, A.L., Hoppe, A., Kester, L., Thompson, B.J., and Tapon, N. (2013). Differential proliferation rates generate patterns of mechanical tension that orient tissue growth. EMBO J. *32*, 2790–2803.

27. Legoff, L., Rouault, H., and Lecuit, T. (2013). A global pattern of mechanical stress polarizes cell divisions and cell shape in the growing Drosophila wing disc. Development *140*, 4051–4059.

28. Pan, Y., Heemskerk, I., Ibar, C., Shraiman, B.I., and Irvine, K.D. (2016). Differential growth triggers mechanical feedback that elevates Hippo signaling. Proc. Natl. Acad. Sci. USA *113*, E6974–E6983.

29. Pellettieri, J., and Sánchez Alvarado, A. (2007). Cell turnover and adult tissue homeostasis: From humans to planarians. Annu. Rev. Genet. *41*, 83–105.

30. Tamori, Y., and Deng, W.-M. (2011). Cell competition and its implications for development and cancer. J. Genet. Genomics *38*, 483–495.

31. Levayer, R., and Moreno, E. (2013). Mechanisms of cell competition: Themes and variations. J. Cell Biol. *200*, 689–698.

32. Di Gregorio, A., Bowling, S., and Rodriguez, T.A. (2016). Cell competition and its role in the regulation of cell fitness from development to cancer. Dev. Cell *38*, 621–634.

33. Amoyel, M., and Bach, E.A. (2014). Cell competition: How to eliminate your neighbours. Development *141*, 988–1000.

34. Honda, H. (1983). Geometrical models for cells in tissues. Int. Rev. Cytol. *81*, 191–248.

35. Gibson, W.T., Veldhuis, J.H., Rubinstein, B., Cartwright, H.N., Perrimon, N., Brodland, G.W., Nagpal, R., and Gibson, M.C. (2011). Control of the mitotic cleavage plane by local epithelial topology. Cell *144*, 427–438.

36. Lee, S.W., and Morishita, Y. (2017). Possible roles of mechanical cell elimination intrinsic to growing tissues from the perspective of tissue growth efficiency and homeostasis. PLoS Comput. Biol. *13*, e1005651.

37. Fletcher, A.G., Osborne, J.M., Maini, P.K., and Gavaghan, D.J. (2013). Implementing vertex dynamics models of cell populations in biology within a consistent computational framework. Prog. Biophys. Mol. Biol. *113*, 299–326.

38. Bosveld, F., Guirao, B., Wang, Z., Rivière, M., Bonnet, I., Graner, F., and Bellaïche, Y. (2016). Modulation of junction tension by tumor suppressors and proto-oncogenes regulates cell-cell contacts. Development *143*, 623–634.

39. Bielmeier, C., Alt, S., Weichselberger, V., La Fortezza, M., Harz, H., Jülicher, F., Salbreux, G., and Classen, A.-K. (2016). Interface contractility between differently fated cells drives cell elimination and cyst formation. Curr. Biol. *26*, 563–574.

40. Oh, H., and Irvine, K.D. (2009). In vivo analysis of Yorkie phosphorylation sites. Oncogene *28*, 1916–1927.

41. Aigouy, B., Farhadifar, R., Staple, D.B., Sagner, A., Röper, J.-C., Jülicher, F., and Eaton, S. (2010). Cell flow reorients the axis of planar polarity in the wing epithelium of Drosophila. Cell *142*, 773–786.

42. Karim, F.D., and Rubin, G.M. (1998). Ectopic expression of activated Ras1 induces hyperplastic growth and increased cell death in Drosophila imaginal tissues. Development *125*, 1–9.

43. Heller, D., Hoppe, A., Restrepo, S., Gatti, L., Tournier, A.L., Tapon, N., Basler, K., and Mao, Y. (2016). EpiTools: An open-source image analysis toolkit for quantifying epithelial growth dynamics. Dev. Cell *36*, 103–116.

44. Curran, S., Strandkvist, C., Bathmann, J., de Gennes, M., Kabla, A., Salbreux, G., and Baum, B. (2017). Myosin II controls junction fluctuations to guide epithelial tissue ordering. Dev. Cell *43*, 480–492.

45. Reddy, B.V.V.G., and Irvine, K.D. (2013). Regulation of Hippo signaling by EGFR-MAPK signaling through Ajuba family proteins. Dev. Cell *24*, 459–471.

46. Hong, X., Nguyen, H.T., Chen, Q., Zhang, R., Hagman, Z., Voorhoeve, P.M., and Cohen, S.M. (2014). Opposing activities of the Ras and Hippo pathways converge on regulation of YAP protein turnover. EMBO J. *33*, 2447–2457.

47. Heisenberg, C.-P., and Bellaïche, Y. (2013). Forces in tissue morphogenesis and patterning. Cell *153*, 948–962.

48. Guirao, B., and Bellaïche, Y. (2017). Biomechanics of cell rearrangements in Drosophila. Curr. Opin. Cell Biol. *48*, 113–124.

49. Kale, A., Rimesso, G., and Baker, N.E. (2016). Local cell death changes the orientation of cell division in the developing Drosophila wing imaginal disc without using fat or dachsous as orienting signals. PLoS ONE *11*, e0167637.

50. Tamori, Y., and Deng, W.-M. (2013). Tissue repair through cell competition and compensatory cellular hypertrophy in postmitotic epithelia. Dev. Cell *25*, 350–363.

51. Aragona, M., Panciera, T., Manfrin, A., Giulitti, S., Michielin, F., Elvassore, N., Dupont, S., and Piccolo, S. (2013). A mechanical checkpoint controls multicellular growth through YAP/TAZ regulation by actin-processing factors. Cell *154*, 1047–1059.

52. Gudipaty, S.A., Lindblom, J., Loftus, P.D., Redd, M.J., Edes, K., Davey, C.F., Krishnegowda, V., and Rosenblatt, J. (2017). Mechanical stretch triggers rapid epithelial cell division through Piezo1. Nature *543*, 118–121.

53. Cong, B., Ohsawa, S., and Igaki, T. (2018). JNK and Yorkie drive tumor progression by generating polyploid giant cells in Drosophila. Oncogene. Published online March 14, 2018. https://doi.org/10.1038/s41388-018-0201-8.

54. Schneider, C.A., Rasband, W.S., and Eliceiri, K.W. (2012). NIH Image to ImageJ: 25 years of image analysis. Nat. Methods *9*, 671–675.

55. Schindelin, J., Arganda-Carreras, I., Frise, E., Kaynig, V., Longair, M., Pietzsch, T., Preibisch, S., Rueden, C., Saalfeld, S., Schmid, B., et al. (2012). Fiji: An open-source platform for biological-image analysis. Nat. Methods *9*, 676–682.

56. Xu, T., and Rubin, G.M. (1993). Analysis of genetic mosaics in developing and adult Drosophila tissues. Development *117*, 1223–1237.

57. Lee, T., and Luo, L. (1999). Mosaic analysis with a repressible cell marker for studies of gene function in neuronal morphogenesis. Neuron *22*, 451–461.

58. Koto, A., Kuranaga, E., and Miura, M. (2009). Temporal regulation of Drosophila IAP1 determines caspase functions in sensory organ development. J. Cell Biol. *187*, 219–231.

59. Umetsu, D., Aigouy, B., Aliee, M., Sui, L., Eaton, S., Jülicher, F., and Dahmann, C. (2014). Local increases in mechanical tension shape compartment boundaries by biasing cell intercalations. Curr. Biol. *24*, 1798–1805.

60. Wartlick, O., Mumcu, P., Kicheva, A., Bittig, T., Seum, C., Jülicher, F., and González-Gaitán, M. (2011). Dynamics of Dpp signaling and proliferation control. Science *331*, 1154–1159.

61. Aigouy, B., Umetsu, D., and Eaton, S. (2016). Segmentation and quantitative analysis of epithelial tissues. Methods Mol. Biol. *1478*, 227–239.

62. Ziosi, M., Baena-López, L.A., Grifoni, D., Froldi, F., Pession, A., Garoia, F., Trotta, V., Bellosta, P., Cavicchi, S., and Pession, A. (2010). dMyc functions downstream of Yorkie to promote the supercompetitive behavior of hippo pathway mutant cells. PLoS Genet. *6*, e1001140.

STAR★METHODS

KEY RESOURCES TABLE

REAGENT or RESOURCE	SOURCE	IDENTIFIER
Antibodies		
rat anti-Drosophila E-cadherin antibody DCAD2	Developmental Studies Hybridoma Bank	Cat# DCAD2; RRID: AB_528120
Chemicals, Peptides, and Recombinant Proteins		
Alexa 647-conjugated phalloidin	Invitrogen	Cat# A22287
4',6-diamidino-2-phenylindole (DAPI)-containing SlowFade Gold Antifade Reagent	Thermo Fisher Scientific	Cat# S36937
Experimental Models: Organisms/Strains		
D. melanogaster: UbxFLP; Act > y+ > Gal4, UAS-GFP; FRT82B, Tub-Gal80	[53]	N/A
D. melanogaster: UbxFLP; FRT42D, Tub-Gal80; Act > y+ > Gal4, UAS-GFP	[53]	N/A
D. melanogaster: UbxFLP; Tub-Gal80, FRT40A; Act > y+ > Gal4, UAS-GFP	[53]	N/A
D. melanogaster: wts^{X1}	Gift from T. Xu	N/A
D. melanogaster: hpo$^{42-47}$	Gift from D.J. Pan	N/A
D. melanogaster: UAS-sqh-RNAi (P{TRiP.HMS00437}attP2)	Bloomington Drosophila Stock Center	BDSC: 32439
D. melanogaster: UAS-shg-RNAi (P{GD14421}v27081)	Vienna Drosophila Resource Center	VDRC: 27081
D. melanogaster: y, w, hs-flp; DE-Cad::GFP; Act > CD2 > GAL4, P{UAS-CD8.mCherry}	This paper	N/A
D. melanogaster: p{tubP-GAL80^{ts}}20	Bloomington Drosophila Stock Center	BDSC: 7019
D. melanogaster: UAS-yki^{S111A,S168A,S250A}:V5	Bloomington Drosophila Stock Center	BDSC: 28817
D. melanogaster: UAS-Ras^{V12}	Gift from T. Xu	N/A
Software and Algorithms		
ImageJ	[54]	N/A
FIJI	[55]	N/A
R	https://www.r-project.org/	N/A
Processing	https://processing.org/	N/A
Other		
Oil compounds	Shin-Etsu	HIVAC-G

CONTACT FOR REAGENT AND RESOURCE SHARING

Further information and requests for resources and reagents should be directed to and will be fulfilled by the Lead Contact, Koichi Fujimoto (fujimoto@bio.sci.osaka-u.ac.jp).

EXPERIMENTAL MODEL AND SUBJECT DETAILS

Drosophila strains and genetics

Strains used for imaging fluorescently-labeled mitotic clones [56, 57] in fixed larval imaginal discs: *UbxFLP; Act > y$^+$ > Gal4, UAS-GFP; FRT82B, Tub-Gal80* (82B tester), *UbxFLP; FRT42D, Tub-Gal80; Act > y$^+$ > Gal4, UAS-GFP* (42D tester), *UbxFLP; Tub-Gal80, FRT40A; Act > y$^+$ > Gal4, UAS-GFP* (40A tester) [53]. Additional strains used were as follows: *wts^{X1}* (from T. Xu), *hpo$^{42-47}$* (from D.J. Pan), *UAS-sqh-RNAi (P{TRiP.HMS00437}attP2)* (Bloomington Stock Center 32439), *UAS-shg-RNAi (P{GD14421}v27081)* (Vienna *Drosophila* Resource Center #27081). Strains used for notum live imaging: *y, w, hs-flp; DE-Cad::GFP; Act > CD2 > GAL4, P{UAS-CD8.mCherry}, p{tubP-GAL80^{ts}}20* (Bloomington Stock Center 7019), *UAS-yki^{S111A,S168A,S250A}:V5* (Bloomington Stock Center 28817), *UAS-Ras^{V12}* (from T. Xu). Crossed offspring for experiments carried a single copy of the transgenes as shown in Experimental genotypes. Both male and female larvae and pupae were used for experiments.

Experimental genotypes

Figures and Videos	Experimental genotype	Developmental stage & tissue
Figures 1A left, 1B, 1C, S1H, and S1I	*UbxFLP; Act > y+ > Gal4, UAS-GFP; FRT82B / FRT82B, Tub-Gal80*	3rd instar Larva, wing disc
Figures 1A right, 1B, 1C, S1H, and S1I	*UbxFLP; Act > y+ > Gal4, UAS-GFP; FRT82B, wtsX1 / FRT82B, Tub-Gal80*	3rd instar Larva, wing disc
Figures 2A, 2C, 2E, 2G, 2H, 2K, 4C, 4G, 4I, 4J, 5B, 5E, 5G, 5J, 5M, 5P, S1J, S4A, S4B, S4C, S4F, S4J, S4K, S4L, and S4M; Videos S1 and S2	*y, w, hs-flp / +; DE-Cad::GFP / p{tubP-GAL80^{ts}}20; Act > CD2 > GAL4, P{UAS-CD8.mCherry} / UAS-yki^{S111A,S168A,S250A}:V5*	Pupa, notum
Figures 2B, 2F, 2I, 2L, 4D, 4H, 5C, 5H, 5K, 5N, 5Q, S1J, S4D, and S4E	*y, w, hs-flp / +; DE-Cad::GFP / P{tubP-GAL80^{ts}}20; Act > CD2 > GAL4, P{UAS-CD8.mCherry} / UAS-Ras^{V12}*	Pupa, notum
Figures S1H and S1I	*UbxFLP; FRT42D / FRT42D, Tub-Gal80; Act > y+ > Gal4, UAS-GFP / UAS-sqh-RNAi (P{TRiP.HMS00437}attP2)*	3rd instar Larva, wing disc
Figures S1H and S1I	*UbxFLP; FRT42D, hpo42-47 / FRT42D, Tub-Gal80; Act > y+ > Gal4, UAS-GFP*	3rd instar Larva, wing disc
Figures S1H and S1I	*UbxFLP; FRT42D, hpo42-47 / FRT42D, Tub-Gal80; Act > y+ > Gal4, UAS-GFP / UAS-sqh-RNAi (P{TRiP.HMS00437}attP2)*	3rd instar Larva, wing disc
Figures S1H and S1I	*UbxFLP; Act > y+ > Gal4, UAS-GFP / UAS-shg-RNAi (P{GD14421}v27081); FRT82B / FRT82B, Tub-Gal80*	3rd instar Larva, wing disc
Figures S1H and S1I	*UbxFLP; Act > y+ > Gal4, UAS-GFP / UAS-shg-RNAi (P{GD14421}v27081); FRT82B, wtsX1 / FRT82B, Tub-Gal80*	3rd instar Larva, wing disc
Figure S1J	*y, w, hs-flp / +; DE-Cad::GFP / P{tubP-GAL80^{ts}}20; Act > CD2 > GAL4, P{UAS-CD8.mCherry} / +*	Pupa, notum

Husbandry conditions

Fly stocks were kept in vials or bottles at 18 or 25°C and transferred every 4 or 3 weeks, respectively. Fly food is a standard corn-sugar-yeast recipe. For cross experiments, healthy adult virgin females and males were placed in a vial and flipped every 1–3 days, and vials containing offspring were raised at 18, 25, or 29°C (see Sections in "METHOD DETAILS" for incubation temperature) until dissection or imaging, unless otherwise stated. For heat shock experiments, vials containing offspring were transiently transferred to 33°C or 34°C for 30 min to induce somatic clones (see Section "Live imaging of pupal notum").

METHOD DETAILS

Immunohistochemistry and fixed-sample imaging

Cross and offspring were kept at 25°C until dissection. We used both male and female larvae for experiments. Larval tissues were stained with standard immunohistochemical procedures using rat anti-*Drosophila* E-cadherin antibody DCAD2 (Developmental Studies Hybridoma Bank (dshb.biology.uiowa.edu), 1:20) and Alexa 647-conjugated phalloidin (Invitrogen, 1:50). Specimens were mounted with 4',6-diamidino-2-phenylindole (DAPI)-containing SlowFade Gold Antifade Reagent (Thermo Fisher Scientific). Images were taken on Leica TCS-SP8 or Zeiss LSM700 confocal microscopes. Images shown in Figures 1A and S1H are sum projections.

Live imaging of pupal notum

Live imaging was performed in the pupal notum rather than the wing disc because the notum does not require *ex vivo* cultivation and is easy to handle. We used both male and female pupae for experiments. Cross and offspring were kept at 18°C for 7–9 days and then subjected to heat shock at 33°C or 34°C for 30 min to induce somatic clones. Larvae were then kept at 18°C. 78.5–81.5 hr or 94–98 hr after heat shock, white prepupae (WPP) were collected. Collected WPPs were transferred to 29°C to express the *UAS-yki^{S111A,S168A,S250A}:V5* transgene, while WPPs were raised for 8 hr at 18°C and transferred to 29°C to express the *UAS-Ras^{V12}* following earlier studies [7]. The pupae were then imaged at 29°C between 15.5–33.5 hr (Yki) or 16–27 hr (Ras^{V12}) after temperature shift. Pupae for image acquisitions were prepared using a modified previously described protocol [58] or [59].

Pupal dissection procedure is as follows:

- Rinse staged pupa with water and dry it on a tissue (e.g., KimWipe). The following procedure is different between protocol [58] or [59].

(Protocol described in [58])

- Mount the washed pupa on a glass slide using double-sided tape.
- Remove the pupal case carefully with forceps at the top of the notum.

- Place filter paper wetted with water around the pupa to avoid desiccation.
- Enclose the pupa with silicon (Shin-Etsu) and place a coverslip on it to seal the pupa.

(Protocol described in [59])

- Paste double-sided tape (upper) to single-sided tape (lower) to enhance the strength by increasing the thickness.
- Mount the washed pupa on the tape.
- Remove the pupal case carefully with forceps at the top of the notum.
- Place the exposed notum directly on a coverslip.

Videos of the nota close to the scutum region were taken on Leica TCS SP5 or SP8 confocal laser scanning microscopes. Z stacks (0.8 μm/slice) were taken every 4 min. Images shown in Figures 2A, 2B, 2C, 4I, 5E, S4D, and S4F and Videos S1 and S2 were maximum projections. For Figures 2B and S4D, the maximum projection was performed by subdividing the picture in 256 × 256-pixel windows to avoid reflecting cuticle wrinkles in the projected image. Tissue-scale images shown in Figures 2A, 2B, 4I, and S4D and Video S1 were processed through the subtract background function in Fiji [55].

Vertex model

The cell-vertex model quantitatively accounts for the packing geometry of normal epithelial cells and predicts the forces that act at cell-cell interfaces, where cell configurations are described as polygons whose vertices form tricellular junctions that are subject to mechanical force [22, 34, 35]. Cells change their shape based on the force balance of cell packing. The primary model used here is represented by the ordinary differential equations of the position vector of each vertex [35]:

$$\frac{d\vec{x_i}}{dt} = F_{tension} + F_{pressure} = \sum_{\langle j \in E(i),\ \alpha \in F(i) \rangle} \left(G_{ij}(d_{ij} - l_0) + \frac{n_H d_{ij}}{A_\alpha} \right) \quad \text{(Equation 1)}$$

E(i) is the set of edges incident to vertex *i*, and *F(i)* is the set of faces to which vertex *i* belongs. The tensional force $F_{tension}$ is exerted to a vertex *i* by the connecting edges between vertices *i* and *j*, where the edge length d_{ij} converges to the preferred length l_0. The internal pressure $F_{pressure}$ is exerted on a vertex *i* by the cell face α to which a vertex *i* belongs, where $F_{pressure}$ increases as the area of cell α (A_α) decreases and the edge length (d_{ij}) increases. The magnitude of $F_{tension}$ and $F_{pressure}$ are controlled by the parameters G_{ij} and n_H, respectively. For all figures in this paper, except for Figures S1F, S1G, S3A–S3G, and S3J (examining the parameter dependency) and Figure S2 (using the other model formulation), the parameter values were set at $G_{ij} = 5$, $l_0 = 0.0001$, and $n_H = 1$. The parameter accounted for cell packing geometry of non-competitive tissue in *Drosophila* (Figures S1A and S1B), and did not dramatically affect the emergence of cell deformation due to differential proliferation rates (Figures S1F, S1G, and S3A–S3C) or asymmetric area expansion induced by apoptosis (Figures S3D, S3F, and S3J).

To test validity of the numerical results independent of the model details, we also examined another vertex model [22] assuming three types of forces, $F_{area\ elasticity}$, $F_{tension}$, and $F_{contractility}$:

$$\begin{cases} \dfrac{d\vec{x}_i}{dt} = F_{area\ elastisity} + F_{tension} + F_{contractility} = -\dfrac{\partial E}{\partial \vec{x}_i} \\ E = \dfrac{1}{2}\sum_\alpha (a_\alpha - 1)^2 + \overline{\Lambda}\sum_{\langle i,j \rangle} l_{ij} + \dfrac{\overline{\Gamma}}{2}\sum_\alpha l_\alpha^2 \end{cases} \quad \text{(Equation 2)}$$

The area elasticity $F_{area\ elasticity}$ is exerted on a vertex *i* by the face α to which a vertex *i* belongs, where area of cell α (a_α) approaches the normalized preferred area of unity. The tension $F_{tension}$ is exerted on a vertex *i* by the connecting edges between vertices *i* and *j*, where $F_{tension}$ increases as the edge length between vertices *i* and *j* (l_{ij}) increases. The contraction $F_{contractility}$ is exerted to a vertex *i* by the contractility of cell perimeter l_α, which is provided by actomyosin contractile force. The parameters were set to $\overline{\Lambda} = 0.06$ and $\overline{\Gamma} = 0.02$ (Figures S1A, S1B, and S2).

Both models (Equation 1 and Equation 2) were integrated numerically using the Euler method with free boundary conditions. To achieve a mechanical equilibrium of tissue state, the position vector of each vertex was calculated after each step until the total velocity of all vertices dropped below a threshold of 1.0. Cell intercalation was incorporated when edges with a length below the threshold 0.001 were maintained for 8.3 × 10^{-4} normalized time [/loser cell cycle], noting that the intercalation during apoptotic cell delamination was introduced independent of this rule (see Section "Apoptosis simulations"). All simulation results were visualized by Processing language (https://processing.org/).

Proliferation in simulations

Each cell divides when the residence time *t* in the cell cycle becomes zero. Total duration of cell cycle obeys gamma distribution with the following probability densities:

$$p(t) = t^{k-1} \frac{\exp\left(-\frac{kt}{\overline{T}}\right)}{(\overline{T}/k)^k \Gamma(k)} \quad \text{(Equation 3)}$$

where $\Gamma(k)$ is the gamma function with $k = 25.0$, following an earlier report [60]. The average and the standard deviation are given by $\overline{T}$ and $\overline{T}/\sqrt{k}$, respectively, with $\overline{T} = 6$ for slower dividing cells ($\overline{T_{slow}}$). In case of the differential proliferation, the average cell cycle of slower dividing cells ($\overline{T_{slow}}$) divided by that of faster dividing cells ($\overline{T_{fast}}$) represents a ratio of the division rates of clones (i.e., $\overline{T_{slow}}/\overline{T_{fast}}$). The simulation time is represented in normalized time [/loser cell cycle], which is divided by $\overline{T_{slow}}$ (loser cell cycle). Although the cell area decreases to half of the original cell area after cell division, it increases subsequently as the cell achieves mechanical equilibrium, following the model formulations (Equation 1 and Equation 2). The orientation of the mitotic cleavage plane obeys the long axis rule [35], where the plane passing through the shorter axis is defined by calculating inertial tensor of each cell using the position of the vertices [37].

Apoptosis in simulations

For apoptosis, several cell intercalation (T1) events were introduced sequentially [7, 24] to incorporate the loss of junctional neighbors (1 intercalation / 1.7×10^{-3} normalized time [/loser cell cycle]). As the apoptotic cell becomes triangular in shape, it is eliminated by the T2 transition [22, 34]. The intercalation was preferentially introduced on the shorter edge of the apoptotic cell, following the probability P_i (except for Figures 6B, S6D, and S6E):

$$P_i = \frac{e^{-\beta l_i}}{\sum_j e^{-\beta l_j}} \qquad \text{(Equation 4)}$$

where l_i and β are the length of edge i and a parameter, respectively. The denominator is a normalization factor of summation of every edge j in an apoptotic cell. P_i for each edge was recalculated at every time before intercalation. The parameters were set to $\beta = 10$ for (Equation 1; except for Figure 7, randomized intercalation) and $\beta = 9.4$ for (Equation 2) to ensure equal probability between of two formulations. For randomized intercalation in Figure 7, we set $\beta = 0$ to provide the same probability for any edge with variable length. Vertex model parameters (G_{ij} and n_H in Equation 1) during the delaminating process were kept constant (delamination type I), except for delamination type II in Figures S3E–S3G. In delamination type II, apical surface of dying cells shrink rapidly by increasing the line tension parameter G_{ij} (Equation 1) and/or decreasing the pressure parameter n_H (Equation 1) before repeated cell intercalation. For the repetitive induction of apoptosis into multiple loser cells in Figures 7 and S7, apoptotic cells were randomly selected from a target region of slower dividing cells. A single apoptosis event occurred every five cell divisions in faster dividing clones.

QUANTIFICATION AND STATISTICAL ANALYSIS

Calculation of cell shape anisotropy

To evaluate cell shape anisotropy, we used two calculation method, "cell anisotropy" and "clone-boundary-oriented cell anisotropy." Cell anisotropy was calculated from the inertial tensor of each cell using the positions of the vertices [37]. The anisotropy α_i of a cell i is represented by the length of long axis l and short axis s calculated from the eigenvalues of the tensor:

$$\alpha_i = \frac{l - s}{l + s} \qquad \text{(Equation 5)}$$

Clone-boundary-oriented cell anisotropy c_i of a cell i is represented by the product of cell anisotropy α_i (Equation 5) and cosine θ_j, angle of its long axis relative to the clone boundary edges j:

$$c_i = \alpha_i \langle cos2\theta_j \rangle_j \qquad \text{(Equation 6)}$$

where $< >_j$ denotes the average for all boundary edges belonging to cell i.

Cell area and shape in fixed-sample imaging

Positions of vertices (junctions) of wild-type cells located at the clone boundary were manually extracted with ImageJ [54] or Fiji [55]. Because epithelial cells in the wing disc are columnar in shape, each vertex was measured at the focal plane of the apical surface, identified by anti-E-cadherin or phalloidin staining. The cell area was calculated from the positions of the vertices by considering a cell a polygon. Strength of cell shape anisotropy was calculated using Equation 5 (Figures 1A, 1B, and S1I).

Image segmentation

Epithelial cells were segmented using Fiji plugin Tissue Analyzer [41, 61].

Segmentation procedure is as follows:

- Save projected video with RGB Color as image sequence (TIF format) with Fiji.
- Launch Tissue analyzer.
- Drag and drop image sequence files into the List.
- Select the channel of adherens junctions (E-cad::GFP).
- Select "Segmentation" tab and click the "Detect Bonds (preview only)" or "Detect bonds V3 (preview only)" and optimize blur values to obtain images with roughly proper segmentation. Click "Detect bonds (save watershed)" or "Detect bonds V3 (save watershed)" to segment all images in the List
- Select "Correction" tab and manually correct the mistakes of the automated segmentation for all images.

- Select "PostProcess" tab and click "Finish all" and "Check finish all" to finalize segmentation.
- Select "Recenter" tab and click "Autocenter based on 2D correction."
- Select "Cell tracking" tab and click "Track cells (dynamics tissue)" to identify the same cells in time. If tracking errors (e.g., cell swapping errors, cell pairing errors) occur, click "Correct/edit cell tracks" and fix them. Click "Check track" and "Update track mask" to finalize cell tracking.
- Select "Virtual cloning" tab to distinguish different types of cells (e.g., wild-type, Yki, Ras^{V12}). Select "Original" and mark cells of interest by left click and click "Drawing -> clone." Click "Check virtual clone" and "Update virtual clone mask" to finalize clone registration.
- Select "Cell divisions" tab and click "Check divisions" and "Update cell division mask" to detect cell division.
- Select "Cell death" tab and click "Track dying cells," "Check death" and "Update cell death mask" to detect cell death.
- Select "Track bonds" tab and click "Track bonds," "Check track bonds" and "Update track bonds" to identify the same bonds (edges) in time.
- Select "SQLite DB" tab and click "Generate/Update database."
- Select "Plots" tab and click "Export cell data" for cell data and "Export bond data" for junction data to save them as csv format.

Apoptosis analysis in live imaging

In this paper, we call "apoptosis" when cells are delaminated from the tissue during live imaging. We therefore do not strictly distinguish delamination "with apoptosis" and "without apoptosis" (i.e., live cell delamination [24]). We expect that the delamination in Yki-induced competition is due, at least in part, to apoptosis, because caspase3-positive wild-type cells are observed during Hippo pathway-induced cell competition [6, 62]. Temporal change in cell area for apoptotic cells and surrounding cells (Figures 2, 4, 5, and S4) was quantified by segmentation and manually identifying cells of interest as "virtual clone" in Fiji plugin Tissue Analyzer [41, 61] (see Section "Image segmentation"). When cells surrounding a dying cell were delaminated or underwent mitosis during quantification (40 min before until 24 min after delamination complete), the contribution of a single apoptotic event on the captured area of surviving neighbors cannot be precisely determined; therefore, we excluded the apoptosis event from the quantification analysis. We also exclude apoptosis inside of the midline [inside of the two most central lines of sensory organ precursors (SOP)], where spontaneous cell delamination occurs independently of cell competition. Cell anisotropy (Figures S4A, S4B, S4C, and S4J) was calculated using Equation 5. Clone-boundary-oriented cell anisotropy (Figures 2J–2L, 5B, 5C, 5G, 5H, and S4J) was calculated using Equation 6.

The normalized frequency of each type of intercalation (Figures 5G, 5H, 5J, 5K, 5M, 5N, 5P, and 5Q) was obtained by dividing the number of occurrences of each intercalation type by the total number of intercalations during a single apoptosis event (Figure 5D). When multiple intercalations (T1 transition) and/or T2 transition take place at a time (during a single time interval: 4 min), the type of cell intercalations were distinguished by estimating intercalated edges from the arrangement of cell neighbor relations. When more than two types of edges are estimated, the probability for occurrences for each intercalation type was calculated as n/n_{ALL} (n: number of estimated edges for a given intercalation type, n_{ALL}: total number of estimated edges). See Figures S4F–S4I for details. Note that, when additional intercalations were observed soon after apoptosis (from 16 to 24 min after delamination complete), the cell topologies were not stably determined; therefore, we excluded the apoptosis events from the current intercalation analysis.

Cell shape, topology, and apoptosis in live imaging

Clonal cells were identified in the Tissue Analyzer and projected onto the segmented image (Figures 2A, 2B, 4I, and S4D). Cell anisotropy (Figures 2A and 2B right, "cell-stretch" in "Viewer" tab), side number (Figures 4I and S4D, "packing-no cutoff" in "Viewer" tab), cell area (Figures 4I and S4D, "image color coder" in "Misc" tab) and apoptosis (Video S1, "apoptotic cells" in "Viewer" tab) were visualized by Tissue Analyzer. For the plots of normalized area as a function of side number (Figures 4J and S4E), we excluded SOPs and their primary neighbors and pupal midline region from the data. In addition, we did not plot data points when the sample number was less than 10. Note that the definition of cell anisotropy in Figures 2A and 2B (see [41]) is different from the one shown in Figures S4A, S4B, S4C, and S5J (see Equation 5) and Figures 2K, 2L, 5B, 5C, 5G, 5H, and S4J (see Equation 6).

Statistical analysis

Scatter plots: Error bars represent standard deviation (s.d.) or standard error (s.e.) of the mean as specified in figure legends. Boxplots: The upper/lower hinge and middle line represent the 25th/75th and 50th percentiles ("boxplot" function in R environment). Statistical test: Fisher's exact test (two-sided), Wilcoxon rank sum test (two-sided), Wilcoxon signed rank test (two-sided), Welch's t test (two-sided, normality and homoscedasticity were tested by Kolmogorov-Smirnov test and F-tests, respectively). Smirnov-Grubbs test was performed to detect outliers (P-values $< 10^{-4}$). Correlation coefficients (described as R in Figures) and significance test were based on Pearson's product-moment correlation coefficient. All calculations and plots were performed with Microsoft Excel or R environment.